The Astrophysical Journal Letters, 940:L43 (18pp), 2022 December 1 https://doi.org/10.3847/2041-8213/aca074

Testing Velocity Kinks as a Planet Detection Method: Do Velocity Kinks in Surface Gas Emission Trace Planetary Spiral Wakes in the Midplane Continuum?

Jessica Speedie[1] and Ruobing Dong (董若冰)[1,2]
[1] Department of Physics & Astronomy, University of Victoria, Victoria, BC V8P 1A1, Canada; jspeedie@uvic.ca
[2] Kavli Institute for Astronomy and Astrophysics, Peking University, Beijing 100871, People's Republic of China; rbdong@uvic.ca
Received 2022 September 20; revised 2022 October 28; accepted 2022 November 1; published 2022 November 29

Abstract

Spiral density waves generated by an embedded planet are understood to cause "kinks" in observed velocity channel maps of CO surface emission by perturbing the gas motion within the spiral arms. If velocity kinks are a reliable probe of embedded planets, we should expect to see the planet-driven spiral arms in other observational tracers. We test this prediction by searching the dust continuum for the midplane counterparts of the spirals responsible for all of the velocity kink planet candidates reported to date whose orbits lie inside the dust continuum disk. We find no clear detection of any spiral structure in current continuum observations for six of the 10 velocity kink planet candidates in our sample (DoAr 25, GW Lup, Sz 129, HD 163296 #2, P94, and HD 143006), despite the high planet masses inferred from the kink amplitude. The remaining four cases include three clear detections of two-armed dust spirals (Elias 27, IM Lup, and WaOph 6) wherein neither spiral arm aligns with a wake originating from a reported planet location, suggesting that under the planetary-origin hypothesis, an accurate method for inferring the location of the planet in the midplane may need to encompass vertical effects. The 10th case, HD 97048, is inconclusive with current knowledge of the disk geometry.

Unified Astronomy Thesaurus concepts: Planetary-disk interactions (2204); Exoplanet detection methods (489); Protoplanetary disks (1300); Planet formation (1241); Exoplanet formation (492)

1. Introduction

The velocity "kink" kinematic signature has gained standing as a promising method for discovering embedded planets (Disk Dynamics Collaboration et al. 2020; Pinte et al. 2022). To date, 12 planet candidates have been reported based on velocity kink detections; in three cases, the planets have been added to the NASA or European exoplanet databases as confirmed planets[3] (Pinte et al. 2019; Izquierdo et al. 2022), and in one case, the candidate's circumplanetary disk has been observed colocated with the kink (AS 209; Bae et al. 2022). Many more such detections of embedded planets are expected with the upcoming exoALMA Large Program.[4]

Some loose ends exist, however, that motivate independent verification of the planetary origin of velocity kinks. Eleven of the 12 velocity kink detections were made in ^{12}CO emission, which is expected to originate above the midplane (e.g., Law et al. 2021), outside of where any analytic theory of velocity kinks has been achieved (Bollati et al. 2021). Ten of the 12 detections were made by visual inspection, without an assessment of the statistical significance of the kink signal (Pinte et al. 2018b, 2019, 2020), and in some cases, the detections do not appear in independent data sets (Teague et al. 2021a). While the planet hypothesis is, on the one hand, supported by the inferred planet locations coinciding with dust gaps, the mass needed to generate kinks with the observed amplitudes is higher than the planet mass derived from the properties of the dust gaps by a factor of 4–100 (e.g., Zhang et al. 2018; Lodato et al. 2019).

The velocity kink signal is understood to be generated by the embedded planet's spiral wakes. Along the spiral arms, the gas motion is perturbed relative to Keplerian rotation, which appears as an excess and absence of emission (i.e., a "kink") in the channel maps (e.g., Bollati et al. 2021). This understanding enables us to make a robust, testable prediction: all instances of planet-driven velocity kinks should be concurrent with planet-driven spiral arms. Recently, Calcino et al. (2022) demonstrated that the velocity kinks observed in ^{12}CO emission in HD 163296 map directly onto the theoretical curve for the spiral wake driven by planet c, projected up onto the emission surface. In this letter, we search the disk midplane for the spiral arms driven by 10 velocity kink planet candidates using (sub) millimeter continuum observations, under the usual assumption that the ∼(sub)millimeter-sized dust traced by such observations has settled to the disk midplane. Our goal is to provide an independent verification for the existence of the predicted planets and thereby test the validity of velocity kinks as signposts of planets in disks.

2. Data and Methods

2.1. Sample: Disks with Velocity Kinks

We compile all of the disks with velocity kinks reported in the literature to date.

1. One kink in HD 163296 (HD 163296 #1) from Pinte et al. (2018b, hereafter Pin18).
2. One kink in HD 97048 from Pinte et al. (2019, hereafter Pin19).
3. Nine kinks (eight new) in eight DSHARP disks, Elias 27, HD 143006, HD 163296 (a second kink in this disk, HD

[3] HD 97048 b (https://exoplanets.nasa.gov/exoplanet-catalog/7503/hd-97048-b/); HD 163296 b (http://exoplanet.eu/catalog/hd_163296_b/); HD 163296 c (http://exoplanet.eu/catalog/hd_163296_c/) .
[4] 2021.1.01123.L; https://www.exoalma.com/.

163296 #2), IM Lup, DoAr 25, GW Lup, Sz 129, and WaOph 6, from Pinte et al. (2020, hereafter Pin20).
4. Two kinks in HD 163296 (a third unique kink, P94, and an independent redetection of HD 163296 #1, dubbed P261) from Izquierdo et al. (2022, hereafter Izq22).
5. One kink in AS 209 colocated with a circumplanetary disk (CPD) candidate from Bae et al. (2022, hereafter Bae22).

In total, 12 velocity kinks have been reported in 10 disks. With the exception of P261 and P94 in HD 163296 (which were identified by `discminer`; Izq22), all of the detections have been made by visual inspection of the channel maps, and the statistical significance of the detections has not been quantified. We list the disks and relevant properties of the kink detections in Table 1.

We then exclude from our sample the detections with inferred planet locations exterior to the outer edge of continuum emission. This eliminates HD 163296 #1, aka P261 (Pin18, Izq22), and AS 209 (Bae22), leaving us with a total of 10 velocity kinks in nine disks (where the repeat disk is HD 163296, containing Pin20's HD 163296 #2 and P94 kinks).

As a side note, velocity deviations attributed to a planet have also been reported in HD 100546 (Casassus & Pérez 2019; Pérez et al. 2020) and TW Hya (Teague et al. 2022). We do not consider these detections in this work primarily[5] because we are concerned with detections based on kinks in velocity channel maps, whereas these were made based on Doppler flips in velocity residual maps.

Planet location. The works reporting the velocity kinks in our sample provide the midplane locations of the predicted planets. As we are testing this prediction, we adopt the given locations. For nine of our 10 candidate planets (the exception being P94 in HD 163296; Izq22), the procedure that was used to determine the planet location is the following (Pin19; Pin20).

1. Identify the CO channel in which the velocity kink is most prominently detected by visual inspection.
2. Identify the center of the kink in that channel by visual inspection.
3. Measure the altitude of the CO emission surface at the center of the kink using the method of Pinte et al. (2018a).
4. Deproject that location onto the disk midplane.

In these nine cases, the planet position is given in sky coordinates (r_p, $\mathrm{PA_p}$) without an estimate of spatial uncertainty.

The location of the P94 planet in HD 163296 is retrieved by `discminer`[6] in disk frame coordinates (R_p, ϕ_p), with an uncertainty in the radial and azimuthal directions of ± 6 au and $\pm 3°$, respectively (Izq22). However, due to `discminer`'s velocity centroid folding procedure,[7] the retrieved polar angle is degenerate about the disk minor axis, and additional information or reasoning is needed to subsequently determine if the detection is on the redshifted or blueshifted side of the disk. The `discminer` velocity residuals of P94 were found to have a Doppler flip morphology, and by reasoning that the sub-Keplerian branch should be interior to the planet's orbit and the super-Keplerian branch should be exterior (Bollati et al. 2021), Izq22 reported the planet on the redshifted side. We note that the "mirror kink" (i.e., the detection with opposite sign but equal significance on the blueshifted side) is colocated with Pin20's HD 163296 #2 kink (footnote 11 of Izq22).

We list the reported locations of the candidate planets in our sample in Table A1. In all cases, the inferred location pinpoints the planet within a dust gap.

2.2. Data Set: Continuum Observations

The continuum data we present in this letter are from the same ALMA program as the CO data in which the velocity kinks were detected. For the eight Pin20 disks, we retrieve the publicly available, self-calibrated, science-ready continuum images and fiducial (continuum-subtracted) $^{12}\mathrm{CO}\ J = 2 - 1$ image cubes from the DSHARP data repository.[8] For HD 97048, we obtain the self-calibrated continuum images and $^{13}\mathrm{CO}\ J = 3 - 2$ cube from Figshare (Pinte 2019). Our analysis is only focused on the continuum images, and we do no new analysis on the CO cubes. Table A2 summarizes the observations and some basic properties of the data. For observational setup and data reduction details, we refer the reader to Pin19 for HD 97048 and Andrews et al. (2018) for the eight DSHARP disks in our sample. We measure the rms noise in the continuum images inside an annulus centered on the disk whose outer radius is the maximum allowed by the field of view and inner radius is sufficiently larger than the source, following Andrews et al. (2018). For reference, we also measure the rms noise in the CO cubes in the same annular area throughout the first and last five channels.

2.3. Methods: Searching for Dust Spirals

Approach. Since spirals are perturbations in surface brightness above/below the background disk, our approach is to subtract an axisymmetric model for the background in order to extract the spiral signal. We create this axisymmetric background model in the image plane by azimuthally averaging the continuum image.

We choose to do our analysis in the image plane, rather than the visibility domain, for two main reasons. First, it yields similar results to *uv*-plane fitting in terms of both the morphology and sensitivity of the residuals and is easily reproducible. We discuss this in more detail in Appendix D.1. Second, the disk conditions (equation of state, optical depth, planet mass) and observing setups (angular resolution, sensitivity) under which the image plane method successfully retrieves the spiral signal have been quantified on synthetic continuum observations of planet-driven dust spirals in hydrodynamic simulations (Speedie et al. 2022). We therefore

[5] Additionally, the HD 100546 planet lies inside a continuum ring ($0\farcs01 \pm 0\farcs04$, $0\farcs21 \pm 0\farcs04$ on the sky; Casassus & Pérez 2019), which is contrary to the classical paradigm that embedded planets carve gaps (though would support the scenario of Nayakshin et al. 2020 and Jiang & Ormel 2022). Since the initial discovery, the velocity deviations in HD 100546 have been explained as being due to an inner binary companion (Norfolk et al. 2022) and disk eruptions driven by an embedded outflow (Casassus et al. 2022). The inferred planet location in TW Hya ($r_p = 1\farcs53$ or 82 au, $\mathrm{PA_p} = 60°$) lies outside of the outer edge of continuum emission that is detected when observed at high angular resolution (~30 mas; Huang et al. 2018a), and the existing observations with sufficient sensitivity to detect continuum emission extending beyond 82 au have a too-low angular resolution for our purposes ($0\farcs37$; Ilee et al. 2022).

[6] We note that `discminer` assesses the significance of a deviation from Keplerian velocity, not whether the deviation matches the expected morphology of a planet-driven velocity deviation (as this has not yet been described analytically in three dimensions).

[7] A way of removing contributions to the velocity field that are symmetric about the disk minor axis, stemming from gas gaps and bulk disk rotation.

[8] https://almascience.eso.org/almadata/lp/DSHARP/

Table 1
Sample and Summary of Possibly Planet-induced Velocity Kink Detections to Date

Disk	Reference	Method	Line	$v_{\rm res}$ (m s^{-1})	$v_{\rm kink\ channel}$ (km s^{-1})	Δv	$\sigma_{\rm kink}$	S/N$_{\rm CO}$	Gap	$M_{\rm p}$ ($M_{\rm Jup}$)	Notes
(1)	(2)	(3)	(4)	(5)	(6)	(7)	(8)	(9)	(10)	(11)	(12)
Kinks Inside the Continuum Emission Disk											
Elias 27	Pin20	VI	^{12}CO(2 − 1)	350	1.70	?	Firm	12	D69	1–3	a
HD 143006	Pin20	VI	^{12}CO(2 − 1)	320	8.84	$\approx$0.2 $v_{\rm Kep}$	Firm	10	D22	1–3	g
HD 163296 (P94)	Izq22	`discminer`	^{12}CO(2 − 1)	320	6.28	0.41 km s^{-1}	(19.4, 7.5)	...	D86	1–3	b
HD 163296 (#2)	Pin20	VI	^{12}CO(2 − 1)	320	3.40	$\approx$0.15 $v_{\rm Kep}$	Firm	36	D86	1–3	b, f
IM Lup	Pin20	VI	^{12}CO(2 − 1)	350	3.05	$<$0.24 $v_{\rm Kep}$	Firm	14	D117	1–3	c
DoAr 25	Pin20	VI	^{12}CO(2 − 1)	350	5.05	?	Tent.	7	D98	1–3	a
GW Lup	Pin20	VI	^{12}CO(2 − 1)	350	2.70	$<$0.3 $v_{\rm Kep}$	Tent.	12	D74	1–3	
Sz 129	Pin20	VI	^{12}CO(2 − 1)	350	4.80	$<$0.2 $v_{\rm Kep}$	Tent.	11	D64	1–3	
WaOph 6	Pin20	VI	^{12}CO(2 − 1)	350	2.10	?	Tent.	13	D79	1–3	a
HD 97048	Pin19	VI	^{13}CO(3 − 2)	120	5.76	...	...	...	130 au	2–3	
Kinks Outside the Continuum Emission Disk											
HD 163296 (#1, P261)	Pin18	VI and `discminer`	^{12}CO(2 − 1)	110	1.00	0.40 km s^{-1}	(5.2, 4.6)[d]	⋯	N/A	2	d, e
AS 209	Bae22	VI	^{12}CO(2 − 1)	200	4.80	⋯	⋯	⋯	N/A	$1.3 \cdot (\alpha/10^{-3})^{1/2}$	

Note. The last two rows are not in our sample, as the inferred planet location lies outside the continuum emission disk, but we include them for completeness. Column descriptions are as follows. (1) Name of disk, with name of kink or planet candidate in parentheses, if applicable. (2) Paper first reporting the velocity kink. All values in the corresponding row are from this reference unless otherwise noted. (3) Method by which the velocity kink was detected. "VI" means visual inspection of the channel maps, and `discminer` is the quantitative tool of Izquierdo et al. (Izq22). (4) CO isotopologue and J transition in which the kink is reported. (5) Velocity (spectral) resolution of the CO cube in which the kink is reported. (6) Velocity (relative to Earth) of the channel in which the kink is most prominently detected, which is used to pinpoint the planet location (see Section 2.1). The two exceptions to this are (i) Izq22 (third row), where the value is one of two channels in which the authors note that the kink can be seen visually (caption of their Figure 1) and `discminer` is used to pinpoint the planet location, and (ii) Bae22 (twelfth row), where the value is the channel in which the CPD candidate is most clearly detected in ^{13}CO and is the central of three channels in which the ^{12}CO velocity kink is reported. (7) Amplitude of the velocity deviation. A question mark means verbatim from the reporting paper, and an ellipsis means not provided by the authors. For an independent velocity deviation prediction from 3D simulations for some of the DSHARP disks, see Rabago & Zhu (2021). (8) Either a qualitative classification as a "firm" or "tentative" kink detection by Pin20 or the statistical significance (σ_r, σ_ϕ) of the deviation from Keplerian velocity from `discminer` (Izq22). (9) Signal-to-noise ratio of CO emission at the location of the kink. (10) Dust gap associated with inferred planet location. The gap name designation is from Huang et al. (2018b) for the DSHARP disks, and the approximate gap radius is in au for HD 97048 (Pin19). (11) Mass estimate of the candidate planet, inferred from the velocity kink amplitude. For the Pin18, Pin19, and Pin20 disks, this is from forward modeling with SPH simulations; for P94, it is from forward modeling with hydrodynamic simulations (Izq22); and for AS 209 (Bae22), it is from the Kanagawa et al. (2016) empirical relation between the gas gap width and planet mass. For mass estimates derived from the dust gap properties, see Zhang et al. (2018) and Lodato et al. (2019). (12) Notes: (a) Channel maps suffer from cloud contamination (column 7 of Table 5 of Andrews et al. 2018). Visually, the affected velocities are 2.75–4.85 km s^{-1} (seven channels) for Elias 27, 1.55–5.05 km s^{-1} (11 channels) for DoAr 25, and 2.45–4.20 km s^{-1} (six channels) for WaOph 6. (b) The HD 163296 #2 and P94 kinks have the same polar angle if mirrored about the disk minor axis (footnote 11 of Izq22). (c) Simulation work supporting the existence of a planet in this disk from Verrios et al. (2022). (d) Value of $\sigma_{\rm kink}$ in this row is from Izq22 with `discminer`. (e) Simulation work supporting the existence of this planet from Calcino et al. (2022). (f) Not verified in ^{12}CO channel maps from the MAPS program (Teague et al. 2021a). (g) Simulation work supporting the existence of this planet from Ballabio et al. (2021).

can form apples-to-apples expectations for the observability of the dust spirals, which we describe in detail in Section 2.4.

Disk geometry. Knowledge of the inclination and position angle of the continuum disk is needed to create the axisymmetric background model, and Table A3 provides the geometrical parameters we use for each disk. For four of the eight DSHARP disks (HD 143006, HD 163296, GW Lup, and Sz 129), we use the values found in Andrews et al. (2021; their Table 2) by the `frank` (Jennings et al. 2020) residual appearance method. We also tried the Huang et al. (2018b) geometries for these four disks and found that they had no effect on our results. For the other four not in Andrews et al. (2021; Elias 27, IM Lup, DoAr 25, and WaOph 6), we use the values found in Huang et al. (2018b; their Table 2) by fitting ellipses to individual annular dust substructures. For HD 97048, no continuum-derived geometry has been published to our knowledge. We thus adopt two possible geometries found by different methods: (i) fitting a Keplerian disk model to the velocity field from CO line data cubes (Table C.1 of Bohn et al. 2022) using `eddy` (Teague 2019a) and (ii) fitting ellipses to rings and gaps in near-IR scattered light (Table 1 of Ginski et al. 2016).

Disk rotation direction. We assume the predicted planet orbits in the same direction that the disk rotates. For HD 163296, DoAr 25, and HD 97048, it has been determined which side of the disk major axis is the near/far side with existing scattered-light observations (see notes for column 10 in Table A3 for references), and we use that information in conjunction with knowing which side about the minor axis is the blue/redshifted side to deduce the direction that the disk rotates. For HD 143006 and GW Lup (low-inclination disks), the near/far side determination is not definitive (e.g., Benisty et al. 2018), but Pérez et al. (2018) suggested that HD 143006's west side is the near side, and Garufi et al. (2022) posited that GW Lup's northwest side is mostly likely the near side. This would mean that HD 143006 rotates clockwise, and GW Lup rotates counterclockwise. In the former case, this happens to be the opposite direction to the "low-level" tentative large-scale Archimedean spiral found by Andrews et al. (2021; see Appendix D.1 for more discussion). For Sz 129, a relatively unstudied disk, no scattered-light observations exist in the literature to our knowledge. Our results (Figures 1 and 2) will show that the rotation direction of these three disks—HD 143006, GW Lup, and Sz 129—is rendered irrelevant by the lack of spiral features in their continuum residual maps, but we still wish to show the tightness of the spiral winding. For that purpose, we assign clockwise for HD 143006 and counterclockwise for GW Lup (motivated by the suggestions of Pérez et al. 2018 and Garufi et al. 2022) and Sz 129 (arbitrarily). For Elias 27, IM Lup, and WaOph 6, we adopt the rotation direction found in Huang et al. (2018c, their Section 3.2).

2.4. Expectations: Dust Spirals Driven by the Velocity Kink Planets

Midplane spiral morphology. We expect the embedded planets predicted by the velocity kink detections to drive spiral wakes in the gas at the midplane whose intrinsic morphology (amplitude, width, and phase) is determined by the planet mass and location, as well as disk temperature.

As we are searching for these spirals in the (sub)millimeter continuum and not the gas, the first question is whether we expect a difference between the dust spiral morphology and the morphology of the spiral in the gas. This depends on how quickly the dust responds to the change in aerodynamic drag forces exerted by the gas when the grains encounter the gas spiral perturbation, which in turn depends on the dust grain size and local gas surface density. Sturm et al. (2020) and Speedie et al. (2022) showed that for dust with a Stokes number ($\mathrm{St} \propto a_{\mathrm{grain}}\,\Sigma_{\mathrm{gas}}^{-1}$, where a_{grain} is the dust grain size, and Σ_{gas} is the local gas surface density) lower than the critical Stokes number, $\mathrm{St} \lesssim \mathrm{St}_{\mathrm{crit}} \approx 0.05$–$0.1$,[9] the dust responds quickly enough such that the resulting dust spiral is morphologically identical to the driving gas spiral at the midplane. We expect our continuum observations to be most sensitive to thermal emission from dust grains of size $a_{\mathrm{grain}} \approx \lambda_{\mathrm{obs}}/2\pi$ (Kataoka et al. 2015; Pavlyuchenkov et al. 2019), which translates to $a_{\mathrm{grain}} \approx 0.14$ mm for HD 97048 (Band 7) and $a_{\mathrm{grain}} \approx 0.20$ mm for the eight DSHARP disks (Band 6). For gas surface densities higher than just $\sim 0.2\ \mathrm{g\ cm^{-2}}$, these grain sizes correspond to Stokes numbers lower than $\mathrm{St}_{\mathrm{crit}}$ (see Figure 2 of Speedie et al. 2022). Figure 7 of Dullemond et al. (2018) shows inferred gas surface densities for a subset of the DSHARP disks (including three in our sample) in the range $0.1\ \mathrm{g\ cm^{-2}} \lesssim \Sigma_{\mathrm{gas}} \lesssim 50\ \mathrm{g\ cm^{-2}}$. To put it another way, assuming a gas surface density profile $\Sigma_{\mathrm{gas}} \sim 1/r$, in order for Σ_{gas} to be lower than $0.2\ \mathrm{g\ cm^{-2}}$ at 50 au (typical location of inner arms in our sample), the total disk mass contained within 100 au would need to be lower than $6.7 \times 10^{-4}\,M_{\odot}$. We therefore expect no difference between the intrinsic morphology of the predicted midplane gas spiral and that of the dust spiral we aim to observe and can use the literature knowledge of gas spirals to understand the morphology of the expected dust spirals.

The trajectory of a planet-driven spiral (i.e., the azimuthal location of the spine, or peak amplitude, as a function of radius) is the result of constructive interference among various spiral wave modes, each excited by a different Fourier component of the planet's gravitational potential (Bae & Zhu 2018a, 2018b). To predict where we expect to see positive residuals (emission above the axisymmetric background) in the continuum residual map for each planet in our sample, we use the analytic phase equation of Bae & Zhu (2018a),[10]

$$\phi_{m,n}(R) = -\phi_{\mathrm{p}} - \mathrm{sgn}(R - R_{\mathrm{p}})\frac{\pi}{4m} + 2\pi\frac{n}{m} - \int_{R_m^{\pm}}^{R} \frac{\Omega(R')}{c_s(R')} \left| \left(1 - \frac{R'^{3/2}}{R_{\mathrm{p}}^{3/2}}\right)^2 - \frac{1}{m^2} \right|^{1/2} \mathrm{d}R',$$

where $(R_{\mathrm{p}}, \phi_{\mathrm{p}})$ are the midplane coordinates of the planet in the disk frame, $\Omega(R)$ is the angular velocity of the disk, $c_s(R)$ is the sound speed of the gas, and m is the azimuthal wavenumber of the wave mode excited by the mth Fourier component of the planet's potential, which itself has a number of components indexed by n. The $n = 0$ components form the primary spiral arms, which are easier to recognize than, e.g., secondary arms ($n = 1$ for $R < R_{\mathrm{p}}$, or $n = m - 1$ for $R > R_{\mathrm{p}}$) because (i) they are launched relatively near to the planet at Lindblad resonances

[9] The critical Stokes number is the Stokes number for which the time it takes a dust grain to cross the spiral wake is equal to the grain's stopping time, so this range is introduced by the azimuthal width of the wake, which changes with planet mass and distance from the planet (Section 3.2 of Speedie et al. 2022).

[10] This equation assumes a circular orbit for the planet; see Fairbairn & Rafikov (2022) and Zhu & Zhang (2022) for the semianalytic linear theory of spiral density waves excited by planets on eccentric orbits.

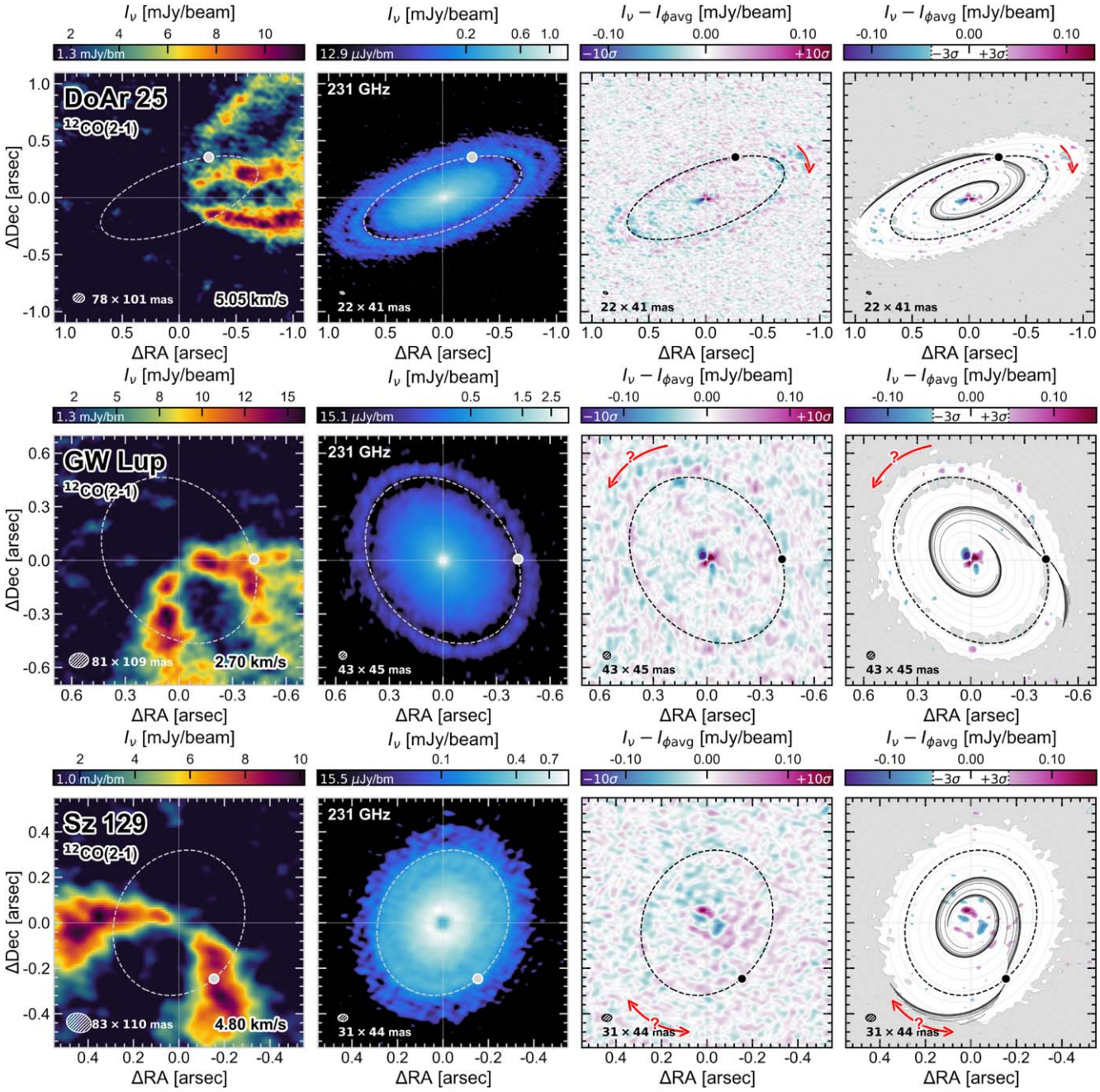

Figure 1. No clear detections of the predicted dust spirals: DoAr 25, GW Lup, and Sz 129. In all columns, the gray or black circle marks the reported planet location in the midplane, and the dashed gray or black line shows its circular orbit. First column: CO channel map in which the velocity kink is most prominently detected. The estimated rms noise in the cube is written in the color bar, and the color map starts at that value. Second column: continuum image showing where the planet lies relative to substructures in the dust distribution. The color map starts at three times the rms noise (again written in the color bar) and has a $\frac{1}{4}$ power-law stretch. Third column: continuum residuals after subtracting the azimuthal average. Red arrows indicate the direction of rotation of the disk, and in all cases, the arrow is located at the redshifted major axis. The color bar spans $\pm 10\times$ the rms noise. Fourth column: comparison between detected residual substructures stronger than $3\times$ the continuum rms noise and the theoretical prediction for the midplane spiral wake driven by the candidate planet (Bae & Zhu 2018a, 2018b; our Equation (1)). Light gray indicates where emission in the continuum image falls below this same threshold, helping to distinguish whether an absence of spiral-shaped residuals is due to the nonpresence of a spiral, or to the nonpresence of emission (e.g., inside dust gaps or beyond the edge of the disk). Thin gray ellipses are projected concentric circles in radial steps of one beam major axis, helping to discern spirals from circular arcs under the angular resolution of the image.

$R_m^{\pm} = (1 \pm 1/m)^{2/3} R_{\rm p}$ (Goldreich & Tremaine 1979), and therefore the inner and outer primary arms always "point" to the planet, whereas the location of the additional arms (both the starting point and the azimuthal separation from the primary) varies with planet mass (Fung & Dong 2015); and (ii) close to the planet, they have the highest amplitude (Bae & Zhu 2018a). As such, we set $n = 0$.

The third term in Equation (1) is the only radially varying term and describes how tightly wound the spiral wave modes are as they propagate away from the planet. In addition to m, this term depends on the gas pressure scale height, $H(R) = c_{\rm s}/\Omega$. We calculate $\Omega(R)$ as the Keplerian angular velocity $\Omega(R) = (G\,M_\star/R^3)^{1/2}$, where R is the disk frame radial coordinate, and $M_\star$ is the stellar mass (column 3,

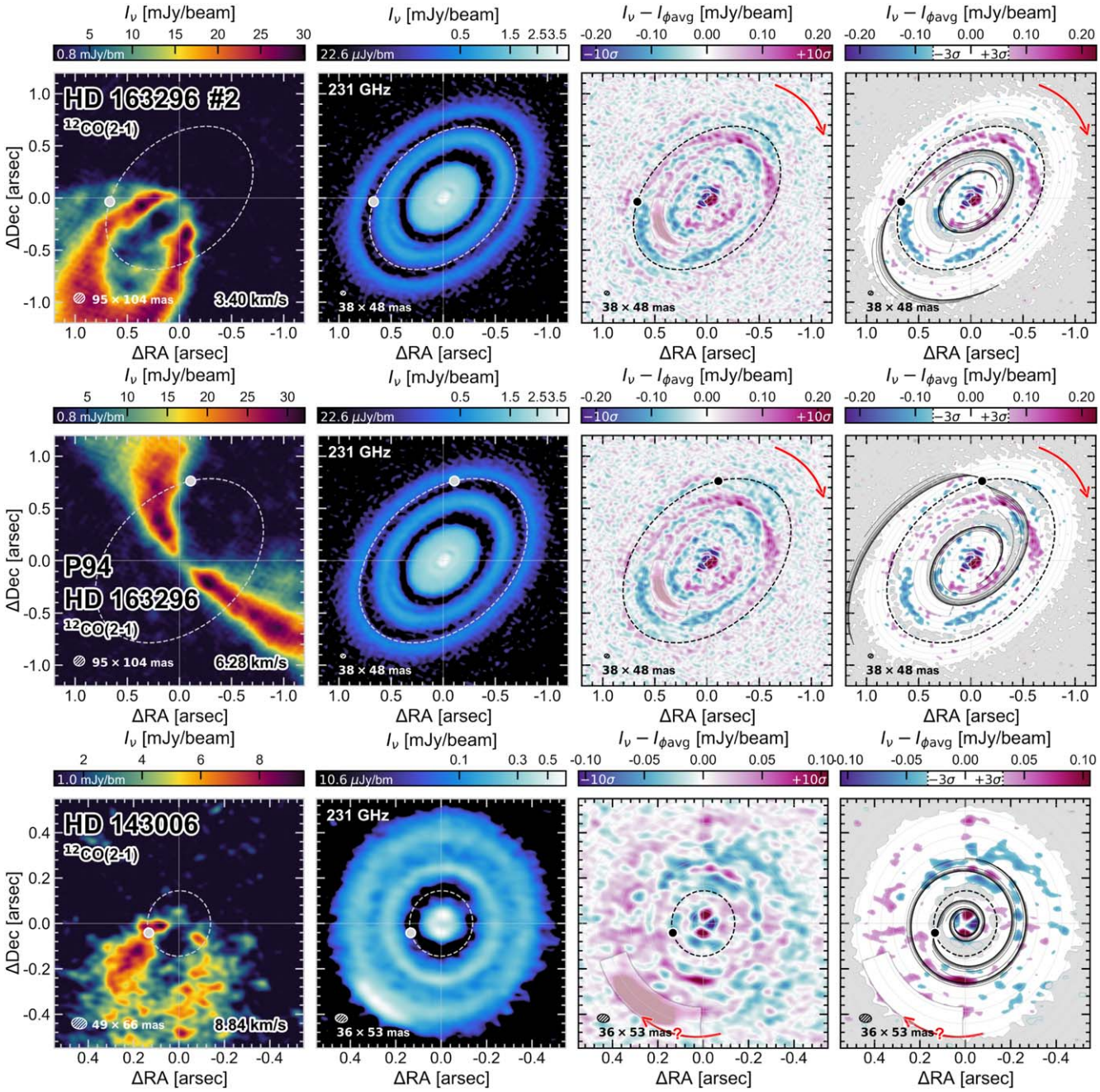

Figure 2. No clear detections of the predicted dust spirals (continued): HD 163296 #2, P94, and HD 143006. We mask the pronounced arc-like azimuthal asymmetries in these two disks to enhance the possibility of spiral detection (see Appendix Figure B1). Additional figures showing the continuum residuals after reimaging the calibrated measurement sets with different Briggs parameters are available for HD 163296, HD 143006, DoAr 25, GW Lup, and Sz 129 at doi:10.6084/m9.figshare.21330426.

Table A3). We calculate the gas sound speed as

$$c_s(R) = \left(\frac{k_B\, T_d(R)}{\mu\, m_{prot}}\right)^{1/2}, \quad (1)$$

where k_B is the Boltzmann constant, $\mu = 2.37$ is the mean molecular weight of the gas in atomic units, and m_{prot} is the proton mass. We thus need an analytic estimate for the disk temperature at the midplane $T_d(R)$, for which we use the simple irradiated flaring disk recipe of Dullemond et al. (2018):

$$T_d(R) = \left(\frac{\frac{1}{2}\varphi L_\star}{4\pi r^2 \sigma_{SB}}\right)^{1/4}. \quad (2)$$

Here $L_\star$ is the luminosity of the central star (column 4, Table A3), σ_{SB} is the Stefan–Boltzmann constant, and φ is the flaring angle (e.g., Chiang & Goldreich 1997; Dullemond et al. 2001). A smaller flaring angle corresponds to a colder

temperature profile and a more tightly wound spiral. We assign $\varphi = 0.02$ to be consistent with Dullemond et al. (2018) and Huang et al. (2018b).

Returning to the m dependence of the third term in Equation (1), we expect the phase of the spiral we see to follow that of the dominant azimuthal mode, $m_{\rm dom} = (\frac{1}{2})(H/r)_{\rm p}^{-1}$, in the case of low-mass planets ($M_{\rm p} \lesssim 0.1\,M_{\rm th}$, where $M_{\rm th} = c_{\rm s}/\Omega G = (H/r)_{\rm p}^{3} M_{\star}$ is the unit of thermal mass; Bae & Zhu 2018a, 2018b). However, for higher-mass planets, the wave modes propagate at faster speeds, and the resulting spiral arms are more open (Goodman & Rafikov 2001) and should more closely follow lower ($m < m_{\rm dom}$) modes. In column 8 of Table A1, we convert the predicted masses of the embedded planets (1–3 $M_{\rm Jup}$; column 8 of Table 1) into units of $M_{\rm th}$ using our estimation of $(H/r)_{\rm p}$ (column 7 of Table A1) and find $M_{\rm p} > 1.0\,M_{\rm th}$ in every case. For this reason, we consider azimuthal wave modes down to the lowest possible m ($m = 1$ in the outer disk and $m = 2$ in the inner disk). We also consider $m \to \infty$, corresponding to the linear limit of Rafikov (2002) and the most tightly wound spirals (used in applications to observations by, e.g., Muto et al. 2012; Casassus et al. 2021).

Observability. Using synthetic continuum observations, Speedie et al. (2022) found that the dust spirals driven by thermal mass planets at 50 au in a slowly cooling and moderately inclined ($i \lesssim 50°$) disk 140 pc away are detectable in continuum observations with sensitivity between 10 and 25 μJy beam^{-1} and angular resolution of ∼30–65 mas. Dong & Fung (2017) showed that the amplitude of the spirals increases with planet mass for subthermal mass planets and flattens out for superthermal mass planets (their Figure 1). In our sample, the inferred planet location is at a few tens to ∼100 au, the mean beam size is $42 \pm 12 \times 54 \pm 17$ mas, the mean distance to the source is 144 ± 26 pc, the estimated continuum rms noises are all $\leqslant$22.6 μJy beam^{-1} (except HD 97048), and only two disks are inclined by greater than 50°. We thus expect the current continuum observations to be sensitive to dust spirals driven by planets of thermal mass and above. Using the estimated $(H/r)_{\rm p}$ (column 7, Table A1) and known $M_{\star}$ (column 3, Table A3) for each candidate in our sample, this $1.0\,M_{\rm th}$ lower limit translates to Jupiter masses ranging between 0.15 and 0.96 $M_{\rm Jup}$ (with $0.15\,M_{\rm Jup}$ corresponding to HD 143006 and $0.96\,M_{\rm Jup}$ to HD 97048).

Note that gravitational instability may also produce spiral arms in continuum emission detectable in ALMA residual maps (Hall et al. 2019) and they may interfere with planet-induced spirals (Rowther et al. 2022). We do not account for this complication in this work.

3. Results and Discussion

We find nondetections of dust spirals for six of the 10 candidate planets in our sample: DoAr 25, GW Lup, Sz 129, HD 163296 #2, P94, and HD 143006 (Figures 1 and 2; Section 3.1). In three cases (Elias 27, IM Lup, and WaOph 6), dust spirals are detected, but their locations do not agree with that of the predicted planet (Figure 4; Section 3.3). For the 10th candidate planet, HD 97048, the result is inconclusive (Figure 3; Section 3.2).

3.1. Nondetections

Of the six nondetections of dust spirals, three correspond to velocity kinks that were classified as "tentative" detections (DoAr 25, GW Lup, and Sz 129; Pin20). In these disks, we find no significant nonaxisymmetric continuum substructure (Figure 1).

Of the other three nondetections (Figure 2), two correspond to "firm" kink detections (HD 163296 #2 and HD 143006; Pin20) and one to a kink detection with a radial and azimuthal significance of $(\sigma_r, \sigma_\phi) = (19.4, 7.5)$ (P94; Izq22). We find some small-scale nonaxisymmetric continuum substructures in these disks, but none that agree with the predicted spiral wakes.

The above results persisted in additional imaging efforts we performed with the calibrated measurement sets for DoAr 25, GW Lup, Sz 129, HD 163296, and HD 143006, varying the Briggs parameter to maximize the observing sensitivity (see Appendix C).

If the planets are there, why do we not see the dust spirals? One possibility is that the disks cool quickly, such that the dust temperature perturbation along the spiral wake is small and does not enhance the spiral's intensity contrast (Speedie et al. 2022; see also Miranda & Rafikov 2020; Zhang & Zhu 2020). If that is the case, then we are mainly only probing the spiral surface density perturbation, which may be washed out at Band 6/7 wavelengths if the optical depth is sufficiently high. Follow-up at longer observing wavelengths may rule this possibility more or less likely. Additionally, in HD 163296 and HD 143006, the planet candidates are embedded in deep gaps and surrounded on either side by narrow rings. Only a small portion of the HD 163296 #2 and P94 spirals have the opportunity to be expressed upon the rings before they encounter the D48 gap or the outer edge of the continuum disk (column 4, Figure 2).

3.2. Inconclusive: HD 97048

We find strong and large-scale continuum residuals for the two assumed geometries (columns 7 and 8, Table A3) for HD 97048 (Figure 3). Significant positive residuals in the inner disk align with the prediction for the inner spiral under both geometries, and the residuals show a portion of the outer spiral under the Ginski et al. (2016) geometry. It is unclear whether these matches support the planet hypothesis or are coincidental, because (a) the quality of the match depends on the geometry assumed, and (b) no matter what geometry we assume, there are significant residuals. Considering the possibility that these strong large-scale residuals indicate that an axisymmetric background model is not a good model, we attempt to find spiral residuals by a method that does not assume axisymmetry (Appendix Figure D3) but come up empty-handed. We thus classify this case as inconclusive.

3.3. Elias 27, IM Lup, and WaOph 6

Of the three detections of dust spirals (Figure 4), two correspond to velocity kinks that were classified as "firm" detections (Elias 27 and IM Lup; Pin20), and one corresponds to a "tentative" kink detection (WaOph 6; Pin20). In all three cases, we see two spiral arms in the continuum residual maps, echoing Pérez et al. (2016) and Huang et al. (2018c).

Comparing the continuum residuals to the predicted spiral trajectories in Figure 4, we find that the locations of the detected dust spirals in these three disks do not match with where we expect them to lie, given the predicted planet locations.

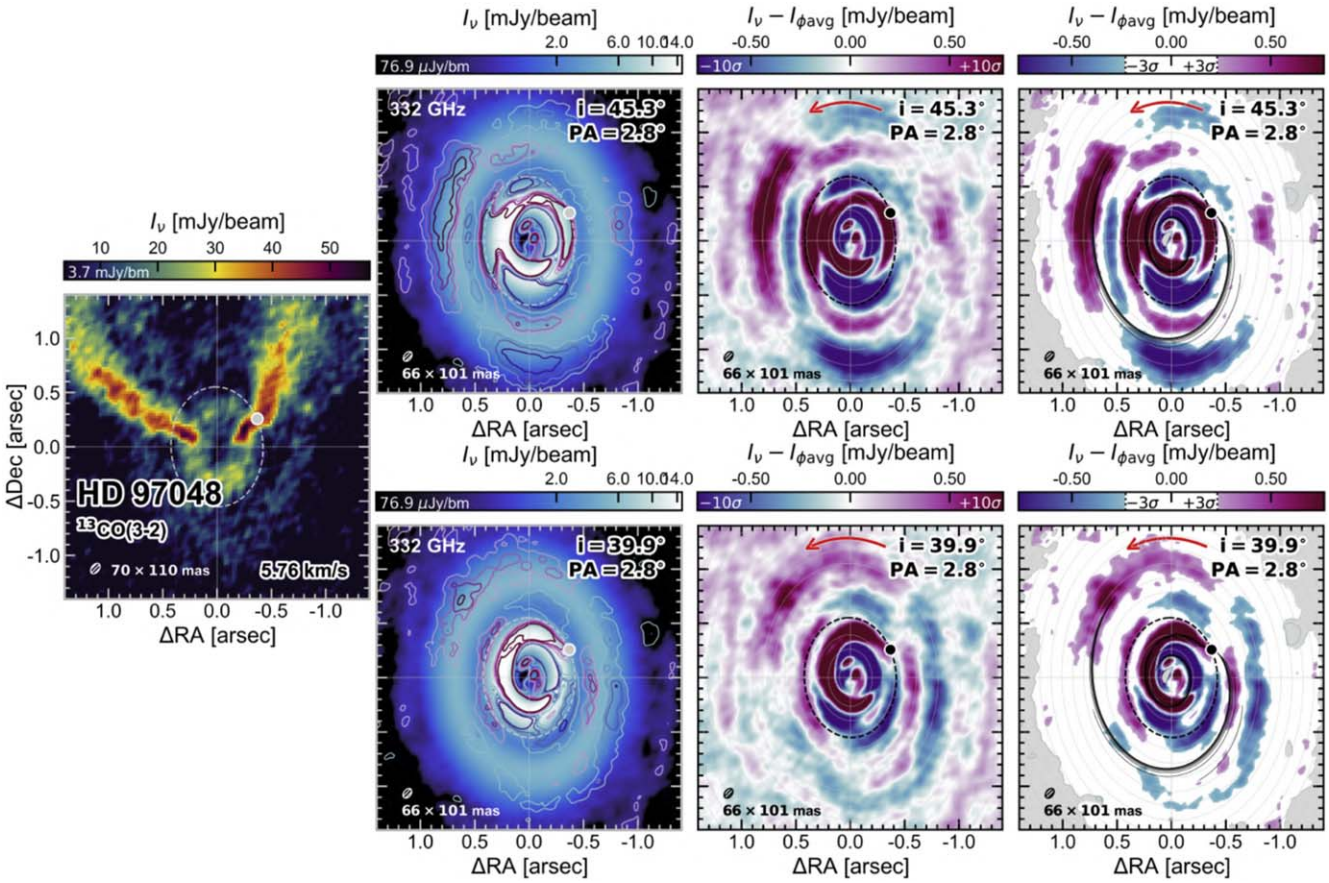

Figure 3. Inconclusive case HD 97048; see Section 3.2 for details. Residual contours of ±3, 5, 7, and 10× the continuum rms noise are overlaid in the second column to help identify where residuals lie in relation to the gap and rings. Top row: continuum residuals calculated assuming the disk geometry of Bohn et al. (2022). Bottom row: continuum residuals calculated assuming the disk geometry of Ginski et al. (2016). Appendix Figure D4 provides non-geometry-dependent residual maps for this disk.

By comparing our estimation of $(H/r)_p$ and the reported estimates of the embedded planet masses (columns 7 and 8, Table A1) to Figure 3 of Bae & Zhu (2018b), we see that the Elias 27, IM Lup, and WaOph 6 planet candidates lie in a region of parameter space where we expect to see both a primary and secondary spiral in the inner disk. This may support the hypothesis that the observed two-armed spirals are planet-driven.

However, the two arms in these three disks are roughly symmetric, and simulations have shown that a planet-to-star mass ratio of $q \sim 0.01$ (or larger) is required to make symmetric inner primary and secondary spiral arms (Figure 3 of Fung & Dong 2015). This is a point of mild tension with the masses inferred from the velocity kink amplitude ($q \in [0.001, 0.005]$ in these three cases). Gravitational instability may be a better explanation for symmetric two-armed spirals (e.g., for Elias 27, see Meru et al. 2017; Tomida et al. 2017; Paneque-Carreño et al. 2021; and for such spirals in other disks, see Dong et al. 2015).

As an alternative possibility that maintains the planetary-origin hypothesis, we contemplate the method used to determine the predicted planet locations (Section 2.1), which involves deprojecting the visually identified kink center location from the estimated emission surface directly onto the midplane. Since the ^{12}CO emission surface is expected to be a few scale heights above the midplane (e.g., Pinte et al. 2018a; Law et al. 2021; Paneque-Carreño et al. 2022), there may be room for error in translation. For example, Zhu et al. (2015) showed with 3D hydrodynamical simulations that spiral wakes are not perpendicular to the midplane and instead curl toward the star at the disk surface. Vertical temperature gradients can introduce further complications, changing a spiral's pitch angle and misaligning the surface wakes from the midplane wakes (Juhász & Rosotti 2018; Rosotti et al. 2020). While Calcino et al. (2022) had success in matching ^{12}CO emission surface kinks around the full disk azimuth to the predicted spiral wake of HD 163296 #1 (P261), their simulations and analytic models assumed no vertical dependence in the velocity perturbations, and the location of this planet (which lies outside the continuum) has not been confirmed in midplane tracers. It is therefore conceivable that the method for pinpointing the planet may need to encompass vertical effects. Motivated by the possibility of leveraging the location of the midplane continuum spirals to inform the development of such a method, we assume that the spirals in Elias 27, IM Lup, and WaOph 6 are planet-driven and explore alternative planet locations.

3.3.1. Considering Alternative Planet Locations

In the following, we present three alternative planet locations (shown left to right in Figure 5) in each of Elias 27, IM Lup, and WaOph 6 under a set of three informative and gradually loosening restrictions. In all cases, the restrictions are based on midplane information: the dust continuum residuals, the

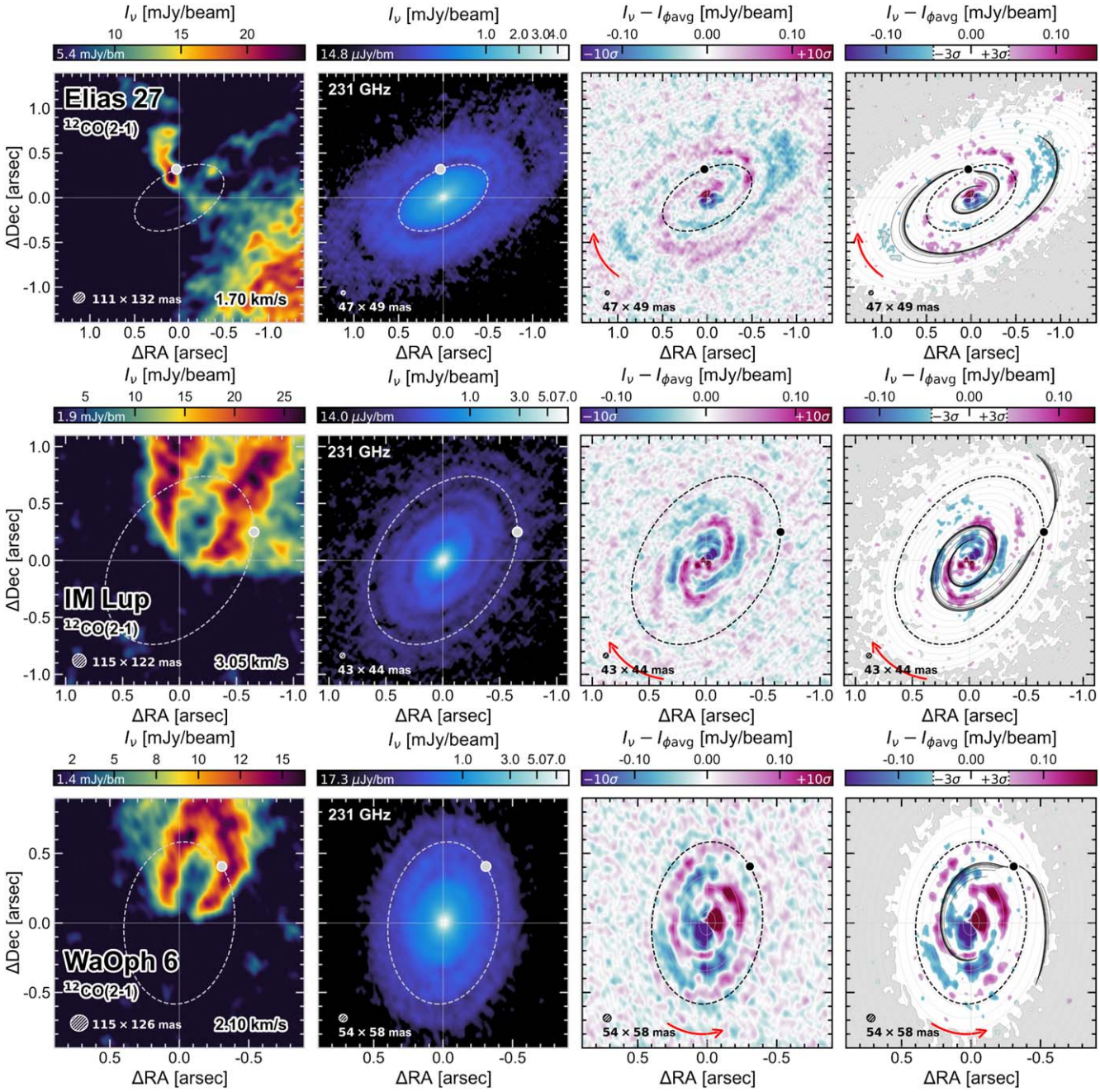

Figure 4. Detections of dust spirals offset from the predicted planet location: Elias 27, IM Lup, and WaOph 6. The continuum spirals in these disks were first reported in Pérez et al. (2016) and Huang et al. (2018c).

deprojected kink location, midplane isovelocity contours, and the 2D velocity kink theory of Bollati et al. (2021). We calculate the midplane isovelocity contours using the 2D Keplerian velocity field $v_0(R, \phi) = v_{\rm Kep}(R)\sin(i)\cos(\phi) + v_{\rm LSR}$, where i is the disk inclination, R and ϕ are the disk frame coordinates (ϕ measured from the redshifted disk major axis), and $v_{\rm LSR}$ is the systemic velocity. For $v_{\rm LSR}$ values, see the notes of Table A4.

In the first column of Figure 5, we shift the planet location to get a better alignment with the detected dust spirals, under the restriction that the planet cannot lie outside the midplane area of the channel in which the velocity kink is most prominently detected. The motivation for this restriction is the idea that the velocity kink amplitude should be strongest close to the planet (e.g., Bollati et al. 2021; Calcino et al. 2022). We represent this area in gray, which spans a half channel width on either side of the velocity of the kink channel[11] (column 6, Table 1) in order to incorporate the spatial "uncertainty" introduced by the spectral resolution of the CO data. We are able to achieve more satisfactory alignments but find that the necessary shift in radial and azimuthal position places the planets outside their DSHARP dust gap (white ellipse in the fourth column).

At the top of Figure 5, we show a midplane schematic of how we may expect the planet location to affect the emission

[11] In the case of Elias 27, we infer from Table 2 and Figure 1 of Pin20 that the kink is also detected in the two adjacent channels, though strong cloud contamination is present. In the cases of Elias 27 and WaOph 6, it is unclear from their Table 2 whether the kink is detected in more than one channel. We thus opt to only consider the single channel.

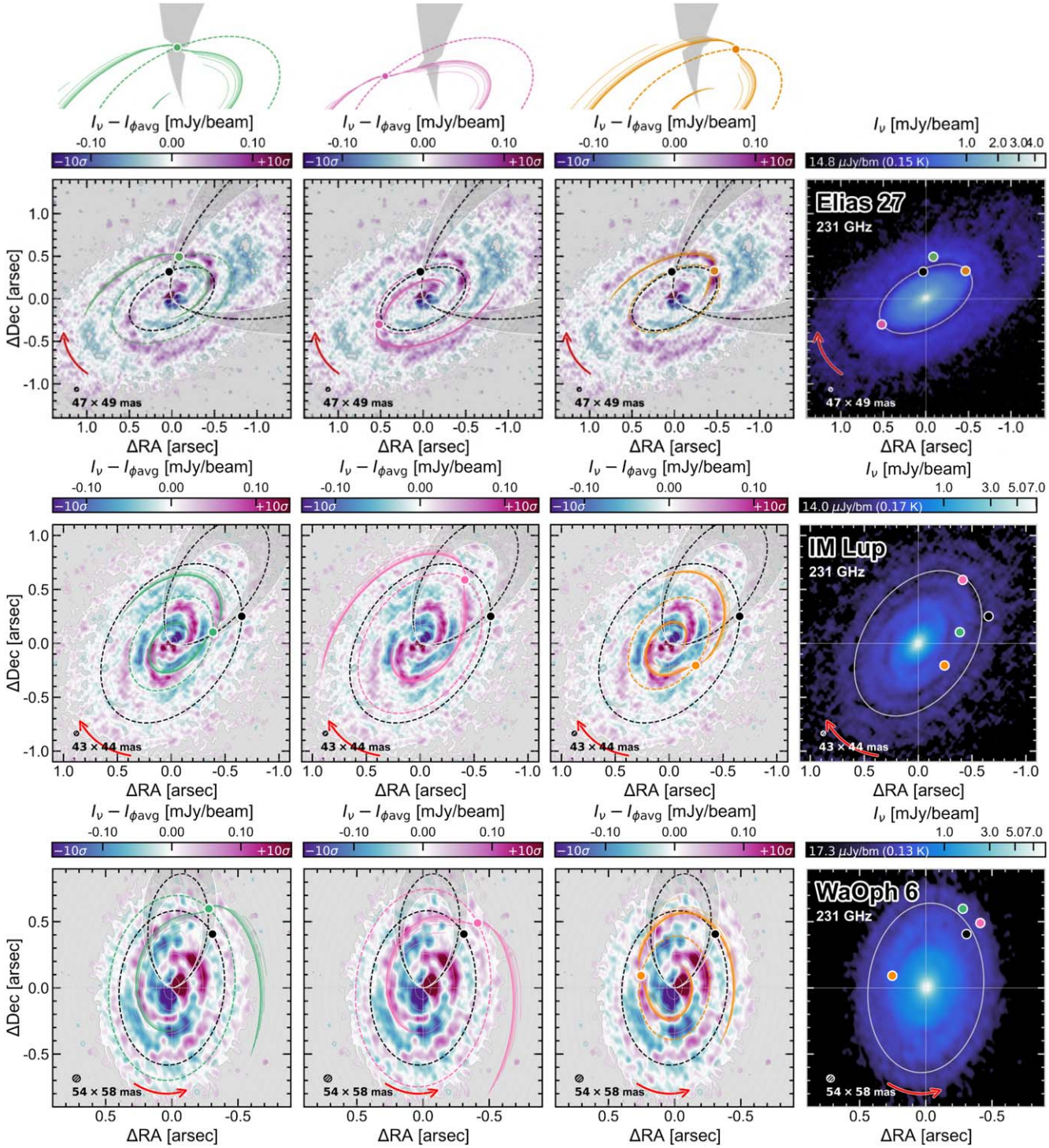

Figure 5. First three columns: alternative planet locations that achieve a better match to the observed continuum spiral residuals in Elias 27, IM Lup, and WaOph 6 under three different restrictions (represented by the schematic at the top of each column; see Section 3.3 for details). The dashed black isovelocity contour is the velocity of the channel in which the kink is most prominently detected, and gray shaded regions demarcate $\pm 0.5\times$ the channel width. In all columns, the black circle marks the deprojected kink location (shown in previous figures as representing the reported planet). Fourth column: comparison between the deprojected kink location and the alternative planet locations. The white ellipse is the DSHARP dust gap associated with the reported planet location (column 10, Table 1).

morphology in a given channel (a logic extension of the results from Bollati et al. 2021): if the inner spiral wake shifts emission to lower velocity channels, and the outer wake shifts emission to higher velocity channels, then the channel centered on the planet may be left with an absence emission at the planet's location. The kink (specifically, emission present in a channel that is spatially offset from the rest) may then instead be most prominent in a channel where it coincides with the inner or outer spiral wake.

Thus, in the second and third columns of Figure 5, we again shift the planet location to get a better alignment with the detected dust spirals, but this time while maintaining that the reported kink is probing a portion of the planet's inner (second column) or outer (third column) spiral arm, with the planet

being as close to the deprojected kink location as possible. Under these two restrictions, we find some qualitative improvement in the match to the detected dust spiral, and in some cases (inner and outer wake scenario for Elias 27, inner wake scenario for IM Lup), we find that the resulting planet location lies inside the DSHARP dust gap. Important to note is that the observed midplane dust spiral residuals do not perfectly intersect with the deprojected kink location (and so the inner and outer wakes of our planet locations do not achieve perfect intersection either), suggesting a possible disjunction between midplane spirals and their expression on the disk surface.

We consider the three planet locations for each disk in Figure 5 to be possible locations in the sense that they plausibly satisfy the continuum spiral residuals. The main caveat is that we have not quantitatively assessed the agreement between the theoretical spiral trajectories and continuum residuals and obtained the planet locations by visual inspection/trial and error. We provide the locations in Table A4 and note that in some cases, the planet in the midplane lies far from the deprojected velocity kink in ^{12}CO surface emission. As mentioned above, our determination of these planet locations was done using midplane-based information without consideration for any surface velocity evidence associated with the new locations, and how the planets can reproduce the strength of the detected kink signals in a distant channel is unclear. It may not be the case that the channel in which the kink is intrinsically most prominent has been correctly identified in Elias 27 and WaOph 6, though, as the ^{12}CO channel maps of these two disks suffer cloud contamination. This applies to almost the entire redshifted (south) half of Elias 27 and a large portion of WaOph 6 from the disk minor axis toward the blueshifted (north) side (see note (a) in Table 1 for affected velocities).

Our results emphasize the need for more theoretical and simulation work to understand the expected morphology of a planet-driven velocity kink, how the planet's spiral manifests at different heights in the disk, how the strength of the kink signal should vary with channel, and how we can use that information to successfully pinpoint the planet.

4. Summary

1. Despite the sufficiently high planet masses inferred from the reported velocity kink amplitudes, we are unsuccessful in detecting any dust spirals associated with six of the 10 velocity kink planet candidates reported to date whose orbits lie within the continuum disk using current continuum observations (Figures 1 and 2). We interpret this to mean that the full planet-finding potential of the velocity kink method may not be exemplified by this specific set of candidates. More kink detection efforts, including better quantification of the kink signal robustness and assessment for a planet-driven morphology, are needed.
2. Our search for dust spirals in the HD 97048 disk is inconclusive (Figure 3). Observations with higher resolution and/or better sensitivity are needed to renew the search.
3. In the remaining three disks in our sample (Elias 27, IM Lup, and WaOph 6), we redetect clear and coherent dust spirals in the continuum residuals (Pérez et al. 2016; Huang et al. 2018c) but find that they do not align with the theoretical spiral trajectory originating at the candidate planet's reported location (Figure 4). If these spirals are planet-driven, then this spatial offset may indicate that the method used to pinpoint the planet location from the kink detection in these disks (Section 2.1) is incomplete; a more successful method may need to encompass how a midplane spiral can be "morphed" during its upward propagation to be expressed on the disk surface (Section 3.3). We provide alternative midplane planet locations that are plausible from the dust spiral's perspective for these three planet candidates in Figure 5 and Table A4, which in some cases are far from the reported velocity kink (Section 3.3.1).

We thank the anonymous referee for the thoughtful and constructive questions and suggestions. J.S. thanks Richard Booth, Cathie Clarke, Giovanni Rosotti, Richard Alexander, Richard Nelson, Brodie Norfolk, Rebecca Nealon, Sahl Rowther, Guilia Ballabio, Simon Casassus, Sebastián Pérez, and Philipp Weber for insightful discussions that helped shape this work, and we thank Daniel Price for comments on the manuscript. J.S. also thanks the curator of the Catalog of Circumstellar Disks (www.circumstellardisks.org). R.D. and J. S. are supported by the Natural Sciences and Engineering Research Council of Canada (NSERC) and the Alfred P. Sloan Foundation.

We are grateful to Christophe Pinte and the DSHARP Collaboration for making their data publicly available. This paper makes use of the following ALMA data: ADS/JAO. ALMA #2016.1.00484.L, ADS/JAO.ALMA #2016.1.00825. S. ALMA is a partnership of ESO (representing its member states), NSF (USA) and NINS (Japan), together with NRC (Canada), MOST and ASIAA (Taiwan), and KASI (Republic of Korea), in cooperation with the Republic of Chile. The Joint ALMA Observatory is operated by ESO, AUI/NRAO and NAOJ. The National Radio Astronomy Observatory is a facility of the National Science Foundation operated under cooperative agreement by Associated Universities, Inc. This work has made use of data from the European Space Agency (ESA) mission Gaia (https://www.cosmos.esa.int/gaia), processed by the Gaia Data Processing and Analysis Consortium (DPAC; https://www.cosmos.esa.int/web/gaia/dpac/consortium). Funding for the DPAC has been provided by national institutions, in particular the institutions participating in the Gaia Multilateral Agreement.

Facility: ALMA.

Software: `astropy` (Astropy Collaboration et al. 2013, 2018), `cmasher` (van der Velden 2020), `disksurf` (Teague et al. 2021b), `gofish` (Teague 2019b), `matplotlib` (Hunter 2007), `numpy` (Harris et al. 2020), `pandas` (The pandas development team 2020), `scipy` (Virtanen et al. 2020).

Appendix A
Tables

Tables A1, A2, A3, and A4.

Table A1
Inferred Midplane Locations of Planets Detected by a Velocity Kink Inside the Continuum

Disk	Reference	Planet Sky Coordinates		Planet Disk Frame Coordinates		$(H/r)_p$	M_p
		r_p (arcsec)	PA_p (deg)	R_p (au)	ϕ_p (deg)		(M_{th})
(1)	(2)	(3)	(4)	(5)	(6)	(7)	(8)
Elias 27	Pin20	$0.32 \pm ...$	$6 \pm ...$	$60 \pm ...$	$-103 \pm ...$	0.087	3.0–8.9
HD 143006	Pin20	$0.14 \pm ...$	$107 \pm ...$	$24 \pm ...$	$-61 \pm ...$	0.043	6.5–19.6
HD 163296 (P94)	Izq22	0.77 ± 0.05	-8 ± 3	94 ± 6	50 ± 3	0.069	1.4–4.3
HD 163296 (#2)	Pin20	$0.67 \pm ...$	$93 \pm ...$	$82 \pm ...$	$129 \pm ...$	0.066	1.6–4.8
IM Lup	Pin20	$0.70 \pm ...$	$-69 \pm ...$	$127 \pm ...$	$136 \pm ...$	0.089	1.5–4.6
DoAr 25	Pin20	$0.44 \pm ...$	$-36 \pm ...$	$101 \pm ...$	$60 \pm ...$	0.071	2.8–8.3
GW Lup	Pin20	$0.42 \pm ...$	$-89 \pm ...$	$78 \pm ...$	$-119 \pm ...$	0.084	3.5–10.4
Sz 129	Pin20	$0.29 \pm ...$	$-148 \pm ...$	$53 \pm ...$	$63 \pm ...$	0.059	5.6–16.8
WaOph 6	Pin20	$0.51 \pm ...$	$-37 \pm ...$	$72 \pm ...$	$138 \pm ...$	0.089	2.0–6.0
HD 97048	Pin19	0.45 ± 0.10	-55 ± 10	109 ± 24	-66 ± 10	0.073	2.1–3.1

Note. Column descriptions are as follows. (1) Name of disk, with name of kink or planet candidate in parentheses, if applicable. (2) Reporting paper, as in Table 1. (3) and (4) Coordinates of the planet as seen on the sky: radial separation from the star (r_p) and position angle measured east of north (PA_p). The ellipsis indicates where authors gave no indication of uncertainty. Note that Pin20 (their Table 1) provided PA_p measured west of north. (5) and (6) Coordinates of the planet in the disk frame: radius in the deprojected midplane (R_p) and polar angle measured counterclockwise from the disk's redshifted major axis (ϕ_p). Disk frame coordinates were calculated by this work, with the exception of the third row (P94; Izq22), in which case we calculated the sky frame coordinates. Values of d used for arcsec $\leftrightarrow$ au are in Table A3. (7) Aspect ratio (H/r) evaluated at R_p, calculated by this work using Equation (2) and $L_\star$ in Table A3. (8) Mass estimate of the planet in units of thermal mass M_{th}, calculated by this work using column 6, $M_\star$ in Table A3, and the M_p range in units of M_{Jup} from the reporting paper (column 11 of Table 1).

Table A2
Summary of Observations Used in This Work

Disk	Origin	CO		Continuum	
		rms Noise (mJy beam^{-1})	θ_{beam} (mas)	rms Noise (μJy beam^{-1})	θ_{beam} (mas)
(1)	(2)	(3)	(4)	(5)	(6)
Elias 27	DDR	1.6	111×132	14.8	47×49
HD 143006	DDR	1.0	49×66	10.7	36×53
HD 163296	DDR	0.8	95×104	22.6	38×48
IM Lup	DDR	1.9	115×122	14.0	43×44
DoAr 25	DDR	1.3	78×101	12.9	22×41
GW Lup	DDR	1.3	81×109	15.1	43×45
Sz 129	DDR	1.0	83×110	15.5	31×44
WaOph 6	DDR	1.4	115×126	17.3	54×58
HD 97048	FS	3.7	70×110	76.9	66×101

Note. Column descriptions are as follows. (1) Name of source. (2) DDR: DSHARP Data Repository (https://almascience.eso.org/almadata/lp/DSHARP/; Program ID: 2016.1.00484.L); FS: Figshare (Pinte 2019); Program ID: 2016.1.00825.S). (3) Measured rms noise in the cube. (4) Synthesized beam FWHM of the cube. (5) Measured rms noise in the image. The values in columns 3 and 5 are almost identical to those of Andrews et al. (2018, Tables 4 and 5) and Pinte et al. (2019). (6) Synthesized beam FWHM of the continuum image.

Table A3
Stellar Properties and Disk Geometries

Disk	d	$M_\star$	$L_\star$	Disk Geometry					Rotation
				Δx	Δy	i	PA	Method	
	(pc)	($M_\odot$)	($L_\odot$)	(mas)	(mas)	(deg)	(deg)		
(1)	(2)	(3)	(4)	(5)	(6)	(7)	(8)	(9)	(10)
Elias 27	110.1 ± 10.3	$0.49^{+0.20}_{-0.11}$	$0.91^{+0.64}_{-0.37}$	-5 ± 5	-8 ± 3	56.2 ± 0.8	118.8 ± 0.7	E	CW
HD 143006	167.3 ± 0.5	$1.78^{+0.22}_{-0.30}$	$3.8^{+1.6}_{-1.1}$	$-6 \pm \sim 2$	$23 \pm \sim 2$	$16 \pm \sim 2$	$167 \pm \sim 2$	FRANK	CW?
HD 163296	101.0 ± 0.4	$2.04^{+0.25}_{-0.13}$	$17.0^{+17}_{-8.5}$	$-3.5 \pm \sim 2$	$4 \pm \sim 2$	$47 \pm \sim 2$	$313 \pm \sim 2$	FRANK	CW
IM Lup	155.8 ± 0.5	$0.89^{+0.21}_{-0.23}$	$2.6^{+1.5}_{-0.95}$	-1.5 ± 2	1 ± 2	47.5 ± 0.3	144.5 ± 0.5	E	CW
DoAr 25	138.2 ± 0.8	$0.95^{+0.10}_{-0.33}$	$1.0^{+0.56}_{-0.35}$	38 ± 2	-494 ± 2	67.4 ± 0.2	290.6 ± 0.2	E	CW
GW Lup	155.2 ± 0.4	$0.46^{+0.12}_{-0.15}$	$0.33^{+0.19}_{-0.12}$	$0.5 \pm \sim 2$	$-0.5 \pm \sim 2$	$39 \pm \sim 2$	$37 \pm \sim 2$	FRANK	CCW?
Sz 129	160.1 ± 0.4	$0.83^{+0.06}_{-0.24}$	$0.44^{+0.26}_{-0.16}$	$5 \pm \sim 2$	$6 \pm \sim 2$	$32 \pm \sim 2$	$153 \pm \sim 2$	FRANK	?
WaOph 6	122.5 ± 0.4	$0.68^{+0.32}_{-0.13}$	$2.9^{+1.7}_{-1.0}$	-244 ± 3	-361 ± 3	47.3 ± 0.7	174.2 ± 0.8	E	CCW
HD 97048	184.4 ± 0.8	2.36 ± 0.19	36.6 ± 20.03	0	0	45.3 ± 2.55	2.84 ± 2.55	Velocity field	CCW
				0	0	39.9 ± 1.8	2.8 ± 1.6	Scattered light	

Note. Column descriptions are as follows. (1) Name of source. (2) Distance to the source from Gaia DR3 (Gaia Collaboration et al. 2016, 2022) as $d = 1/\varpi$. (3) Stellar mass. (4) Stellar luminosity. Values for $L_\star$ and $M_\star$ are from Andrews et al. (2018), except for HD 97048, in which case $L_\star$ and $M_\star$ are from Bohn et al. (2022). (5) R.A. offset of disk center from phase center (in the data sets we use; see Table A2). (6) Decl. offset of disk center from phase center. (7) Disk inclination. (8) Disk position angle, measured counterclockwise (i.e., east of north) to the redshifted major axis. (9) Method used to estimate disk position angle, inclination, and offset from phase center in the work from which we source the values: "E" indicates that the values were derived by fitting ellipses to continuum annular substructures (Table 2, Huang et al. 2018b); "FRANK" indicates the `frank` residual appearance method of Andrews et al. (2021, their Table 2); "velocity field" indicates the results of fitting a Keplerian disk model to the velocity field from CO line data cubes (Table C.1, Bohn et al. 2022) with `eddy` (Teague 2019a); and "scattered light" indicates the results of fitting ellipses to gaps and rings observed in near-IR scattered light by SPHERE (Table 1, Ginski et al. 2016). (10) Direction in which the disk rotates, where "CW" means clockwise (west of north), and "CCW" means counterclockwise. Rotation directions for Elias 27 and WaOph 6 were taken from Huang et al. (2018c); the remaining disk rotations were determined by this work based on scattered-light observations in the following works: Elias 27 (Huang et al. 2018c), HD 143006 (Benisty et al. 2018; Pérez et al. 2018), HD 163296 (Monnier et al. 2017; Muro-Arena et al. 2018), IM Lup (Avenhaus et al. 2018; Huang et al. 2018c), DoAr 25 (Andrews et al. 2008; Garufi et al. 2020), GW Lup (Garufi et al. 2022), Sz 129 (none to our knowledge), WaOph 6 (Huang et al. 2018c), HD 97048 (Ginski et al. 2016). A question mark indicates cases where the near/far side is uncertain or unknown in scattered-light images in the literature to date (note the low inclination of those three disks).

Table A4
Coordinates of the Alternative Planet Locations Presented in Figure 5

Disk	Col.	Sky Coordinates		Disk Frame Coordinates		v_p
		r_p	PA_p	R_p	ϕ_p	
		(arcsec)	(deg)	(au)	(deg)	(km s^{-1})
(1)	(2)	(3)	(4)	(5)	(6)	(7)
Elias 27	1	0.50	−10	85	−114	1.65
	2	0.60	120	66	2	4.48
	3	0.57	−55	64	191	0.31
IM Lup	1	0.40	−75	76	129	2.99
	2	0.72	−35	112	−179	2.51
	3	0.32	−130	74	87	4.57
WaOph 6	1	0.66	−25	86	153	2.13
	2	0.64	−40	92	135	2.53
	3	0.27	70	48	−100	3.40

Note. Column descriptions are as follows. (1) Name of disk. (2) Column of Figure 5 showing the planet whose coordinates are given, numbered 1–3, left to right. (3) and (4) Coordinates of the planet as seen on the sky: radial separation from the star (r_p) and position angle measured east of north (PA_p). (5) and (6) Coordinates of the planet in the disk frame: radius in the deprojected midplane (R_p) and polar angle measured counterclockwise from the disk's redshifted major axis (ϕ_p). Values of d used for arcsec ↔ are in Table A3. (7) Velocity coordinate of the planet relative to Earth. The systemic velocities used to find these values were estimated from the morphology of emission in the channel maps (thus having uncertainty v_{sys}; column 5 of Table 1) and are $v_{LSR} = 2.40$ km s^{-1} for Elias 27, $v_{LSR} = 4.45$ km s^{-1} for IM Lup, and $v_{LSR} = 3.85$ km s^{-1} for WaOph 6.

Appendix B
Treatment of Confined Azimuthal Asymmetries

The strong emission from the confined arc-like features in HD 163296 and HD 143006 will, of course, raise the azimuthal average emission within the radial region that they occupy, therefore making it more difficult to detect any dust spirals above the (overly positive) average background in that radial region. This is particularly relevant for our search in HD 163296, as the inner spiral wake of both the HD 163296 #2 and P94 planets would be expressed upon the B67 ring, which

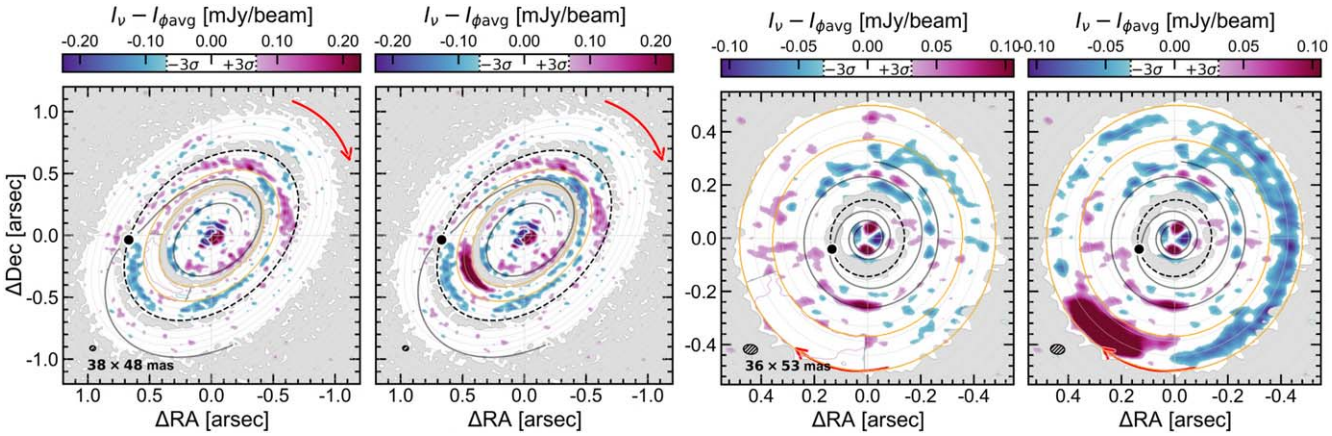

Figure B1. Treatment of crescents in HD 163296 and HD 143006: detected residual substructures stronger than 3× the continuum rms noise in HD 163296 (left two panels) and HD 143006 (right two panels) when either including or excluding the confined arc-like azimuthal asymmetries. The two orange ellipses guide the eye to the radial region affected (i.e., the residual maps are identical outside of this region). A 3σ contour of the arc-like feature is shown under the mask to demonstrate how the mask covers the feature.

is contaminated by the arc-like feature. It is less important for our search in HD 143006 because the candidate planet's spiral wake is tightly wound and unlikely to "reach" the radial region occupied by the crescent. In HD 163296, we omit from the calculation of the azimuthal average the emission lying within $135^\circ \leqslant \phi \leqslant 220^\circ$ between $R = 0\farcs49$ and $0\farcs63$, where R and ϕ are disk frame coordinates (ϕ measured counterclockwise from the redshifted disk major axis). In HD 143006, we omit the emission lying within $-58^\circ \leqslant \phi \leqslant 12^\circ$ between $R = 0\farcs37$ and $0\farcs5$.

Figure B1 shows the continuum residual maps in HD 163296 and HD 143006 with and without including the confined arc-like features in the azimuthal average. In HD 163296, excluding the arc-like feature modifies the residuals in a way that is more relevant for the HD 163296 #2 planet candidate than for P94 (hence why it is plotted in Figure B1 instead of P94); some disconnected positive residuals are introduced in the northeast portion of the radial region (where HD 163296 #2's inner spiral would lie), though they do not appear to be a segment of a spiral. In HD 143006, excluding the arc-like feature removes the strongly negative residuals in the western half of the disk but does not affect the residuals near the planet candidate.

Appendix C
Reimaging the Continuum Visibilities to Achieve Higher Sensitivity

Speedie et al. (2022) argued that a beam size ∼twice as large as the width of the spiral can yield a higher signal-to-noise ratio detection in a residual map than a higher angular resolution image. Motivated by this, we reimaged the publicly available DSHARP calibrated measurement sets of the five disks whose fiducial images yielded nondetections (DoAr 25, GW Lup, Sz 129, HD 163296, and HD 143006), varying the Briggs parameter to explore the full available range of angular resolutions and achievable sensitivities. We show an example of the results in Figure C1. The full set is available at doi:10.6084/m9.figshare.21330426.

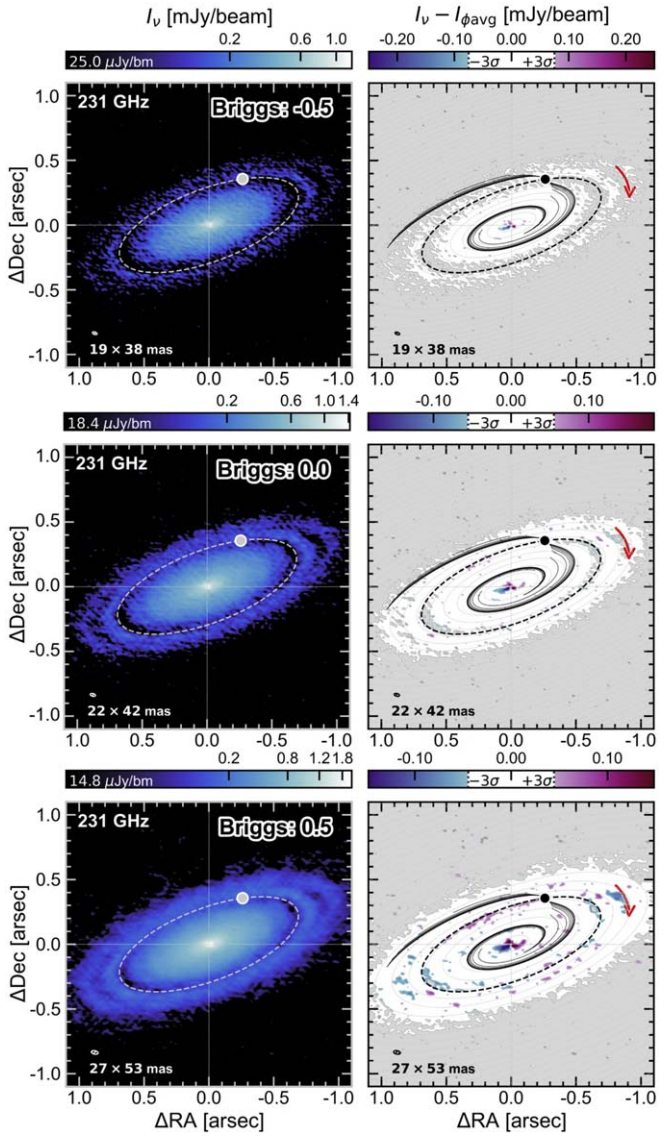

Figure C1. Subset of our reimaging efforts with higher Briggs parameters to increase the beamwidth and sensitivity, showing the disk DoAr 25 as an example. The full set of images for DoAr 25, Sz 129, GW Lup, HD 163296, and HD 143006 for Briggs parameters $\in[-1, -0.5, -0.3, 0, 0.3, 0.5, 1, 2]$ is available at doi:10.6084/m9.figshare.21330426.

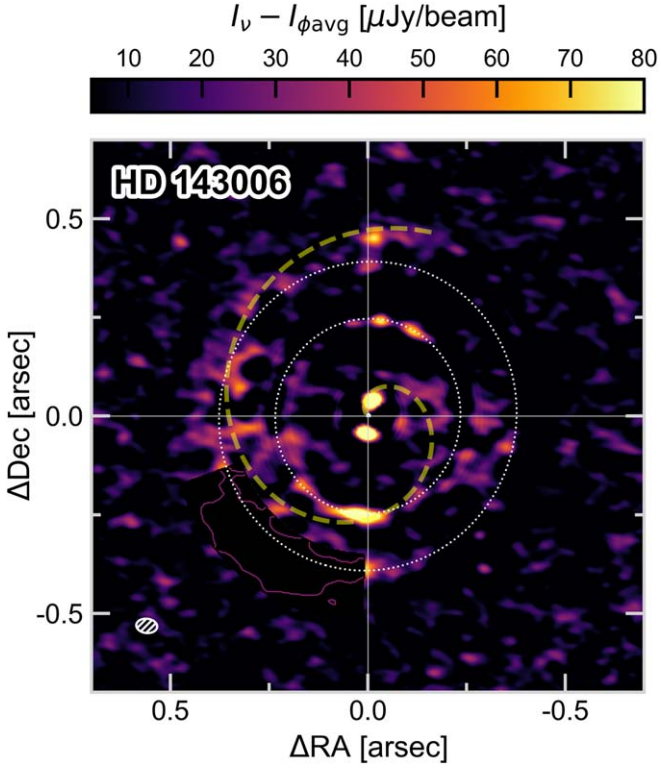

Figure D1. Representation of our azimuthal average continuum residual map for HD 143006 for comparison to Figure 4 of Andrews et al. (2021). The dashed yellow curve is their (visually tuned, not fit) Archimedean spiral overlay, described in disk frame coordinates by $R_{\rm spiral} = 0.170 + 0.067\phi$ [arcsec]. The two dotted white ellipses mark the DSHARP-identified rings, B41 and B65.

Appendix D
Methods for Detecting Dust Spirals

D.1. Comparison with `frank`

All eight of the DSHARP disks in our sample were analyzed in *uv*-space with `frank` by Jennings et al. (2022a), and four of them were also analyzed by Andrews et al. (2021). Those works did not report detections of dust spirals in the `frank` residual maps of DoAr 25, GW Lup, Sz 129, and HD 163296, a result echoed by this letter. Side-by-side comparisons between the imaged `frank` residuals and our image plane residuals show that the techniques give nearly identical results.

Andrews et al. (2021) reported a "low-level" tentative large-scale Archimedean spiral in HD 143006 (their Figure 4). In our Figure D1, we represent the continuum residuals we obtained for HD 143006 (the exact same map as appears in the main text in the bottom right panel of Figure 2) on the same color scale as Andrews et al. (2021) to more clearly demonstrate the extent to which our azimuthal average technique recovers this tentative spiral. The basic result is similar, and our method recovers the spotty residual features along the Andrews et al. (2021) spiral. In this case, some differences in the residuals can be attributed to the differing treatments of the confined azimuthal asymmetries. We note that the direction of this spiral (assuming it is trailing) implies counterclockwise rotation for the HD 143006 disk, opposite to the clockwise rotation suggested by Pérez et al. (2018).

D.2. Additional Searches with the Unsharp Masking Method

One of the most significant challenges to using the azimuthal average as a background model is that it makes assumptions on the disk geometry—namely, that the dust disk is inherently axisymmetric and planar, and that one has accurate knowledge of the disk inclination and position angle. Artificial residuals can be introduced if one uses the incorrect disk geometry. Creating residual maps with `frank` (Jennings et al. 2020) involves the same challenges (e.g., Appendix A of both Andrews et al. 2021 and Jennings et al. 2022b).

In this section, we explore an alternative technique that makes no assumptions on the disk geometry and apply it to the disks that exhibited small- or large-scale azimuthal average residuals: HD 163296, HD 143006, and HD 97048. The technique has been referred to as "unsharp masking" (e.g., Pérez et al. 2016; Meru et al. 2017) and involves convolving the observation with a

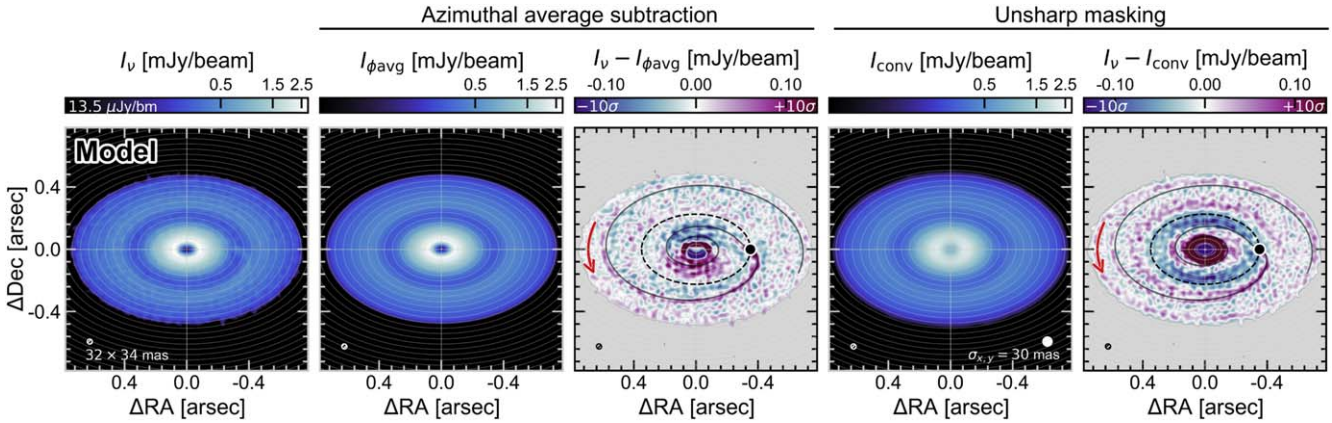

Figure D2. Comparing methods for detecting planet-driven dust spirals: azimuthal average subtraction versus unsharp masking. First panel: synthetic continuum observation, I_ν. Second panel: background disk model $I_{\phi\ \mathrm{avg}}$ obtained by azimuthally averaging I_ν using knowledge of the disk inclination, position angle, and phase offset. Third panel: residual map as the difference between I_ν and $I_{\phi\ \mathrm{avg}}$. Fourth panel: background disk model I_{conv} obtained by convolving I_ν with a 2D Gaussian kernel of HWFM $\sigma_{x,y}$, making no assumptions on the disk geometry. The filled white circle represents the Gaussian kernel. Fifth panel: residual map as the difference between I_ν and I_{conv}. In the residual maps, we overlay the theoretical prediction for the midplane spiral wake driven by the model planet (Bae & Zhu 2018a, 2018b; our Equation (1)), whose mass is $M_\mathrm{p} = 1.0\,M_\mathrm{th}$. Only the dominant azimuthal mode ($m_\mathrm{dom} = (\frac{1}{2})(H/r)_\mathrm{p}^{-1}$) is shown, and the planet's outer spiral wake becomes more open than the predicted trajectory with distance from the planet.

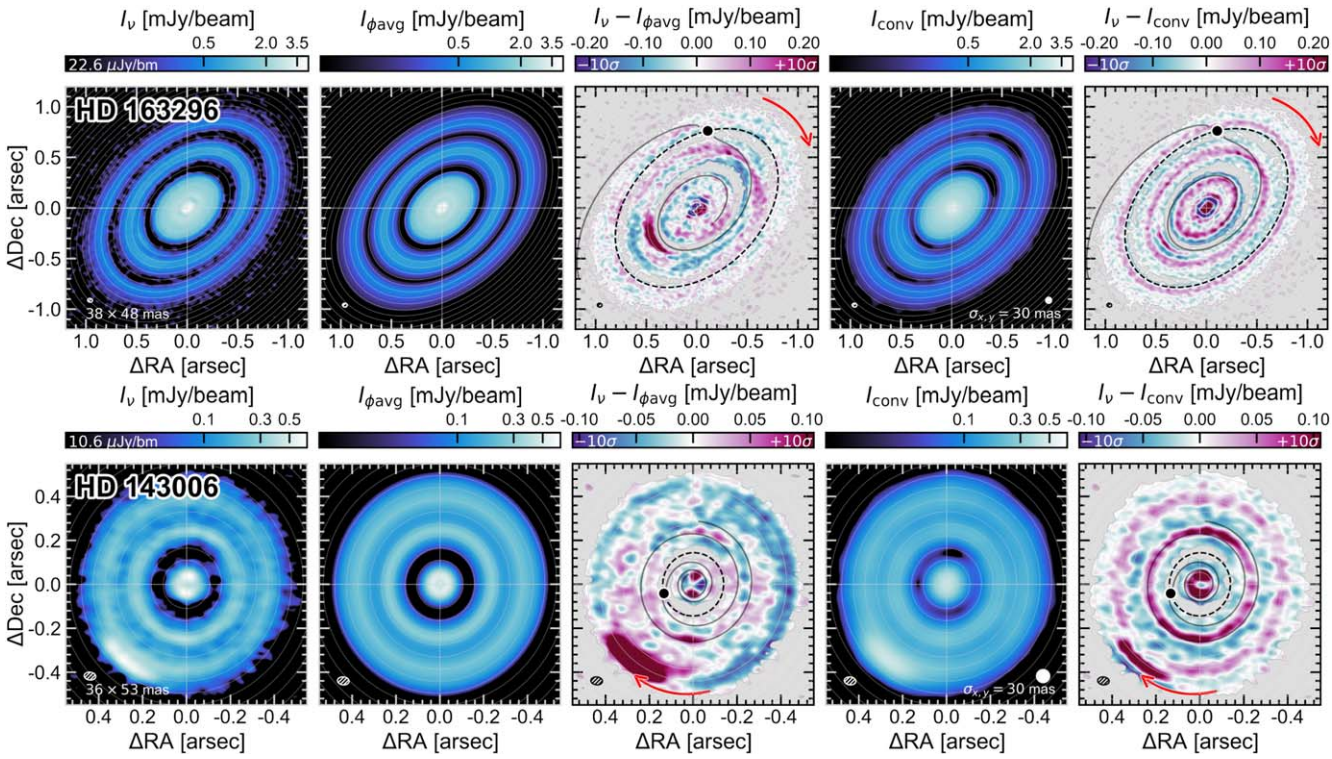

Figure D3. Additional searches for the predicted dust spirals: HD 163296 and HD 143006. The panel layout is similar to Figure D2.

normalized 2D Gaussian of HWFM $\sigma_{x,y}$ and subtracting the result from the original image. It is mathematically equivalent to the "high-pass filtering" technique (e.g., Rosotti et al. 2020; Norfolk et al. 2022), which involves suppressing large-scale spatial (angular) frequencies by convolution with a 1D Gaussian of HWFM σ_ν in the Fourier domain. We confirmed that both give identical residual maps with the appropriately scaled Gaussian kernels ($\sigma_\nu = 2\pi/\sigma_{x,y}$) but only show the former here so as to consistently work in the image plane.

Figure D2 compares the efficacy of the residual-making method we use in the main body of the paper to that of the unsharp masking method using a synthetic continuum observation model[12] from Speedie et al. (2022). To produce the unsharp masking residual map, we convolve the model image (I_ν; first panel) with a 2D Gaussian of HWFM $\sigma_{x,y} = 30$ mas (I_{conv}; fourth panel) using `scipy.ndimage.Gaussian_filter`. The residuals resulting from different kernel

[12] Downloadable from Figshare: doi:10.6084/m9.figshare.21330426. This model contains a 1.0 M_th mass planet at 50 au in an adiabatic, slowly cooling ($\beta = 10$), marginally optically thin ($\tau_0 = 0.3$) disk at a distance of 140 pc, observed with the C5+C8 ALMA configuration pair for an on-source time of 3.56 hr.

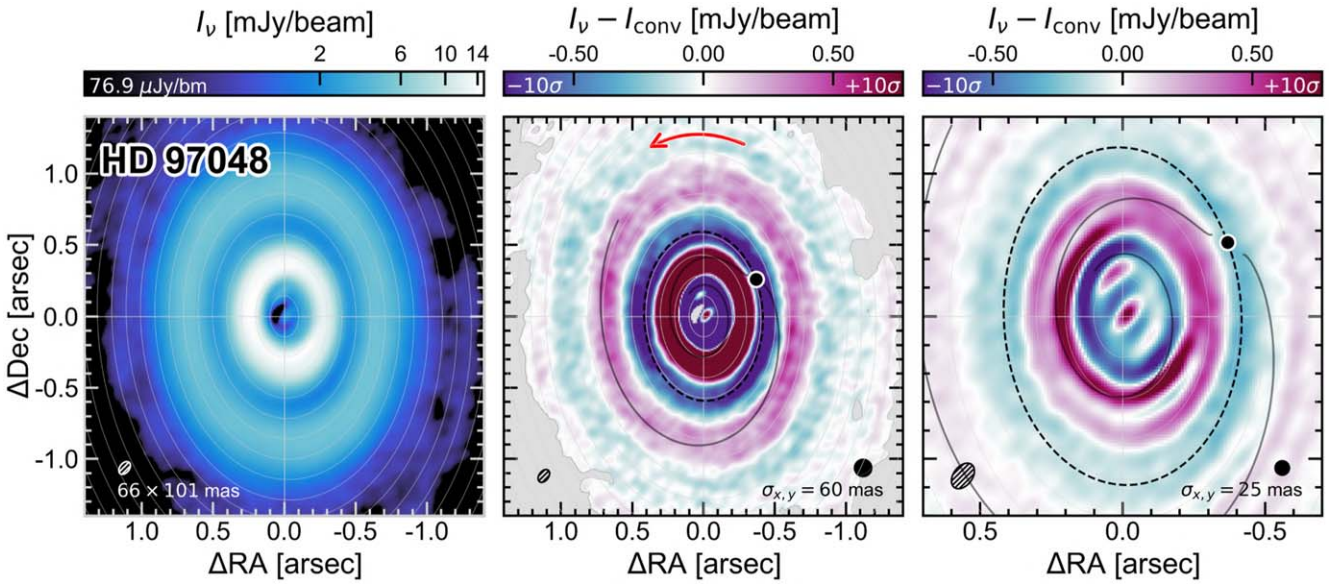

Figure D4. Additional searches for the predicted dust spirals: HD 97048. Unsharp masking residuals are produced with two 2D Gaussian kernels of different sizes to highlight substructure in the outer (second panel) and inner (third panel) rings.

sizes will vary in morphology, as different kernels sequentially highlight different spatial scales of the image structures, and in practice, we strongly encourage the observer to view the results for a range of $\sigma_{x,y}$. Here we show the results for a select $\sigma_{x,y}$, chosen such that I_{conv} is smoothed of blobs but still contains the radial structure present in I_ν. This figure shows that the unsharp masking method can be effective, though it is prone to accentuating gaps and rings.

Nonetheless, for its main benefit of not requiring assumptions on the disk geometry, we apply it to the continuum observations of HD 163296, HD 143006, and HD 97048 in Figures D3 and D4. In the resulting residual maps for HD 163296 and HD 143006 (fifth column of Figure D3), we detect only ring and gap structures and no spirals, consistent with the azimuthal average method in the main text. In HD 97048 (Figure D4), we find that a single 2D Gaussian kernel does not highlight substructure in both the inner and outer ring simultaneously, so we show the results for both a $\sigma_{x,y} = 60$ mas kernel and a $\sigma_{x,y} = 30$ mas kernel. The residual map produced with the larger kernel (second panel of Figure D4) shows no spiral structure in the outer ring. The residual map produced with the smaller kernel (third panel of Figure D4) reveals a double-ring structure over $\sim 270^\circ$ of the inner ring but no residuals that consistently follow the predicted trajectory for the planet's inner spiral arm.

ORCID iDs

Jessica Speedie https://orcid.org/0000-0003-3430-3889
Ruobing Dong (董若冰) https://orcid.org/0000-0001-9290-7846

References

Andrews, S. M., Elder, W., Zhang, S., et al. 2021, ApJ, 916, 51
Andrews, S. M., Huang, J., Pérez, L. M., et al. 2018, ApJL, 869, L41
Andrews, S. M., Hughes, A. M., Wilner, D. J., & Qi, C. 2008, ApJL, 678, L133
Astropy Collaboration, Price-Whelan, A. M., Sipőcz, B. M., et al. 2018, AJ, 156, 123
Astropy Collaboration, Robitaille, T. P., Tollerud, E. J., et al. 2013, A&A, 558, A33
Avenhaus, H., Quanz, S. P., Garufi, A., et al. 2018, ApJ, 863, 44
Bae, J., Teague, R., Andrews, S. M., et al. 2022, ApJL, 934, id.L20
Bae, J., & Zhu, Z. 2018a, ApJ, 859, 118
Bae, J., & Zhu, Z. 2018b, ApJ, 859, 119
Ballabio, G., Nealon, R., Alexander, R. D., et al. 2021, MNRAS, 504, 888
Benisty, M., Juhász, A., Facchini, S., et al. 2018, A&A, 619, A171
Bohn, A. J., Benisty, M., Perraut, K., et al. 2022, A&A, 658, A183
Bollati, F., Lodato, G., Price, D. J., & Pinte, C. 2021, MNRAS, 504, 5444
Calcino, J., Hilder, T., Price, D. J., et al. 2022, ApJL, 929, L25
Casassus, S., Cárcamo, M., Hales, A., Weber, P., & Dent, B. 2022, ApJL, 933, L4
Casassus, S., Christiaens, V., Cárcamo, M., et al. 2021, MNRAS, 507, 3789
Casassus, S., & Pérez, S. 2019, ApJL, 883, L41
Chiang, E. I., & Goldreich, P. 1997, ApJ, 490, 368
Disk Dynamics Collaboration, Armitage, P. J., Bae, J., et al. 2020, arXiv:2009.04345
Dong, R., & Fung, J. 2017, ApJ, 835, 38
Dong, R., Hall, C., Rice, K., & Chiang, E. 2015, ApJL, 812, L32
Dullemond, C. P., Birnstiel, T., Huang, J., et al. 2018, ApJL, 869, L46
Dullemond, C. P., Dominik, C., & Natta, A. 2001, ApJ, 560, 957
Fairbairn, C. W., & Rafikov, R. R. 2022, MNRAS, 517, 2121
Fung, J., & Dong, R. 2015, ApJL, 815, L21
Gaia Collaboration, Prusti, T., de Bruijne, J. H. J., et al. 2016, A&A, 595, A1
Gaia Collaboration, Vallenari, A., Brown, A. G. A., et al. 2022, arXiv:2208.00211
Garufi, A., Avenhaus, H., Pérez, S., et al. 2020, A&A, 633, A82
Garufi, A., Dominik, C., Ginski, C., et al. 2022, A&A, 658, A137
Ginski, C., Stolker, T., Pinilla, P., et al. 2016, A&A, 595, A112
Goldreich, P., & Tremaine, S. 1979, ApJ, 233, 857
Goodman, J., & Rafikov, R. R. 2001, ApJ, 552, 793
Hall, C., Dong, R., Rice, K., et al. 2019, ApJ, 871, 228
Harris, C. R., Millman, K. J., van der Walt, S. J., et al. 2020, Natur, 585, 357
Huang, J., Andrews, S. M., Cleeves, L. I., et al. 2018a, ApJ, 852, 122
Huang, J., Andrews, S. M., Dullemond, C. P., et al. 2018b, ApJL, 869, L42
Huang, J., Andrews, S. M., Pérez, L. M., et al. 2018c, ApJL, 869, L43
Hunter, J. D. 2007, CSE, 9, 90
Ilee, J. D., Walsh, C., Jennings, J., et al. 2022, MNRAS, 515, L23
Izquierdo, A. F., Facchini, S., Rosotti, G. P., van Dishoeck, E. F., & Testi, L. 2022, ApJ, 928, 2
Jennings, J., Booth, R. A., Tazzari, M., Clarke, C. J., & Rosotti, G. P. 2022a, MNRAS, 509, 2780
Jennings, J., Booth, R. A., Tazzari, M., Rosotti, G. P., & Clarke, C. J. 2020, MNRAS, 495, 3209
Jennings, J., Tazzari, M., Clarke, C. J., Booth, R. A., & Rosotti, G. P. 2022b, MNRAS, 514, 6053
Jiang, H., & Ormel, C. W. 2022, arXiv:2207.13002
Juhász, A., & Rosotti, G. P. 2018, MNRAS, 474, L32
Kanagawa, K. D., Muto, T., Tanaka, H., et al. 2016, PASJ, 68, 43

Kataoka, A., Muto, T., Momose, M., et al. 2015, ApJ, 809, 78
Law, C. J., Teague, R., Loomis, R. A., et al. 2021, ApJS, 257, 4
Lodato, G., Dipierro, G., Ragusa, E., et al. 2019, MNRAS, 486, 453
Meru, F., Juhász, A., Ilee, J. D., et al. 2017, ApJL, 839, L24
Miranda, R., & Rafikov, R. R. 2020, ApJ, 892, 65
Monnier, J. D., Harries, T. J., Aarnio, A., et al. 2017, ApJ, 838, 20
Muro-Arena, G. A., Dominik, C., Waters, L. B. F. M., et al. 2018, A&A, 614, A24
Muto, T., Grady, C. A., Hashimoto, J., et al. 2012, ApJL, 748, L22
Nayakshin, S., Tsukagoshi, T., Hall, C., et al. 2020, MNRAS, 495, 285
Norfolk, B. J., Pinte, C., Calcino, J., et al. 2022, ApJL, 936, L4
Paneque-Carreño, T., Miotello, A., van Dishoeck, E. F., et al. 2022, arXiv:2210.01130
Paneque-Carreño, T., Pérez, L. M., Benisty, M., et al. 2021, ApJ, 914, 88
Pavlyuchenkov, Y., Akimkin, V., Wiebe, D., & Vorobyov, E. 2019, MNRAS, 486, 3907
Pérez, L. M., Benisty, M., Andrews, S. M., et al. 2018, ApJL, 869, L50
Pérez, L. M., Carpenter, J. M., Andrews, S. M., et al. 2016, Sci, 353, 1519
Pérez, S., Casassus, S., Hales, A., et al. 2020, ApJL, 889, L24
Pinte, C. 2019, HD 97048 ALMA B7 continuum + 13CO, FigShare, doi:10.6084/m9.figshare.8266988.v1
Pinte, C., Ménard, F., Duchêne, G., et al. 2018a, A&A, 609, A47
Pinte, C., Price, D. J., Ménard, F., et al. 2018b, ApJL, 860, L13
Pinte, C., Price, D. J., Ménard, F., et al. 2020, ApJL, 890, L9
Pinte, C., Teague, R., Flaherty, K., et al. 2022, arXiv:2203.09528
Pinte, C., van der Plas, G., Ménard, F., et al. 2019, NatAs, 3, 1109
Rabago, I., & Zhu, Z. 2021, MNRAS, 502, 5325
Rafikov, R. R. 2002, ApJ, 569, 997
Rosotti, G. P., Benisty, M., Juhász, A., et al. 2020, MNRAS, 491, 1335
Rowther, S., Nealon, R., & Meru, F. 2022, MNRAS, 518, 763
Speedie, J., Booth, R. A., & Dong, R. 2022, ApJ, 930, 40
Sturm, J. A., Rosotti, G. P., & Dominik, C. 2020, A&A, 643, A92
Teague, R. 2019a, JOSS, 4, 1220
Teague, R. 2019b, JOSS, 4, 1632
Teague, R., Bae, J., Aikawa, Y., et al. 2021a, ApJS, 257, 18
Teague, R., Bae, J., Andrews, S. M., et al. 2022, ApJ, 936, 163
Teague, R., Law, C., Huang, J., & Meng, F. 2021b, JOSS, 6, 3827
The pandas development team 2020, pandas-dev/pandas: Pandas 1.4.2, Zenodo, doi:10.5281/zenodo.3509134
Tomida, K., Machida, M. N., Hosokawa, T., Sakurai, Y., & Lin, C. H. 2017, ApJL, 835, L11
van der Velden, E. 2020, JOSS, 5, 2004
Verrios, H. J., Price, D. J., Pinte, C., Hilder, T., & Calcino, J. 2022, ApJL, 934, L11
Virtanen, P., Gommers, R., Oliphant, T. E., et al. 2020, NatMe, 17, 261
Zhang, S., & Zhu, Z. 2020, MNRAS, 493, 2287
Zhang, S., Zhu, Z., Huang, J., et al. 2018, ApJL, 869, L47
Zhu, Z., Dong, R., Stone, J. M., & Rafikov, R. R. 2015, ApJ, 813, 88
Zhu, Z., & Zhang, R. M. 2022, MNRAS, 510, 3986